APL Materials

REVIEW ARTICLE | DECEMBER 06 2021

Solution-processed metal oxide dielectric films: Progress and outlook

Won-June Lee ; Taehyun Kwak; Jun-Gyu Choi; Sungjun Park ; Myung-Han Yoon

APL Mater. 9, 120701 (2021)
https://doi.org/10.1063/5.0066014

Solution-processed metal oxide dielectric films: Progress and outlook

Cite as: APL Mater. 9, 120701 (2021); doi: 10.1063/5.0066014
Submitted: 7 August 2021 • Accepted: 18 November 2021 •
Published Online: 6 December 2021

Won-June Lee,[1] Taehyun Kwak,[2] Jun-Gyu Choi,[1] Sungjun Park,[2,a)] and Myung-Han Yoon[1,a)]

AFFILIATIONS

[1] School of Materials Science and Engineering, Gwangju Institute of Science and Technology, Gwangju 61005, Republic of Korea
[2] Electrical and Computer Engineering, Ajou University, Suwon 16499, Republic of Korea

[a)] **Authors to whom correspondence should be addressed:** sj0223park@ajou.ac.kr and mhyoon@gist.ac.kr

ABSTRACT

There has been growing interest in the use of the sol-gel approach to form high-quality dielectric materials. Their tailored properties allow for developing functional electronic devices in a scalable and rapid manner. According to physicochemical principles, the displacement and response behavior of charges under an applied external field can manifest in unique dielectric properties, providing useful information to improve the process, design, and quality of electronic devices. Therefore, a systematic and in-depth investigation of the fundamentals of sol-gel dielectrics is necessary. In this Research Update, we present recent advances in various sol-gel-processed dielectric materials and their applications to functional electronic devices. A brief introduction to sol-gel chemistry to form oxide dielectric films and the basis of physical mechanisms under electrical fields are discussed. Along with the dielectric properties, recent achievements of proof-of-concept experiments and their various applications to functional electronic devices are introduced. It is expected that further innovations in solution-processed metal oxide dielectrics will achieve cost-effective high-performance functional electronics in the near future.

I. INTRODUCTION

Since the studies of Ebelman and Graham[1] on the formation of silica-based materials from chemical solutions in the mid-1800s, considerable advancements in the sol-gel method have been made for the synthesis of functional metal oxides, including a broad range of applications.[2] For applications in major components of electronic devices, conventional sol-gel processes follow a reaction pathway of hydrolysis, condensation, and gelation[3] from metal precursor solutions to form thin metal oxide films. The desired structures and properties of metal oxide materials can be tailored[3,4] according to controllable synthetic conditions, such as the types of precursors (salts or alkoxide); solvent (alcohol or aqueous solvent); stirring, aging time, or both; temperature, pH, and additives; and subsequent annealing at a high temperature (typically above 400 °C). Completing the reaction results in a metal–oxide–metal (M–O–M) network, eliminating organic impurities and unreacted chemical residues and promoting densification, crystallization, or both of the resultant oxide films. Currently, the sol-gel process is considered to be one of the most promising fabrication routes to form high-quality metal oxide electronic materials with good uniformity, large scalability, and cost efficiency. To illustrate the process overview and various strategies of the solution-processed metal oxide dielectric films, Fig. 1 provides four major process steps in sequence: (I) solution synthesis, (II) film deposition, (III) treatment process, and (IV) device fabrication for various applications.

A dielectric is an electrical insulator composed of non-conducting materials susceptible to the electric field (E-field). They offer a wide range of useful properties for functional electronic devices, such as thin-film transistors (TFTs),[4–9] resistive switching (RS) memory,[10,11] ferroelectric memory,[12–14] synaptic devices for neuromorphic function,[15,16] and even energy storage devices.[17,18] Dielectric properties can be classified according to the polarization behavior under an applied E-field, as shown in Fig. 2. Conventional dielectric materials exhibit linear dielectric polarization behavior proportional to the applied external E-field owing to their lack of permanent dipoles. Paraelectric materials without ferroelectric domains exhibit a slightly nonlinear P–E curve caused by the displacement of permanent dipoles, including the polarization of

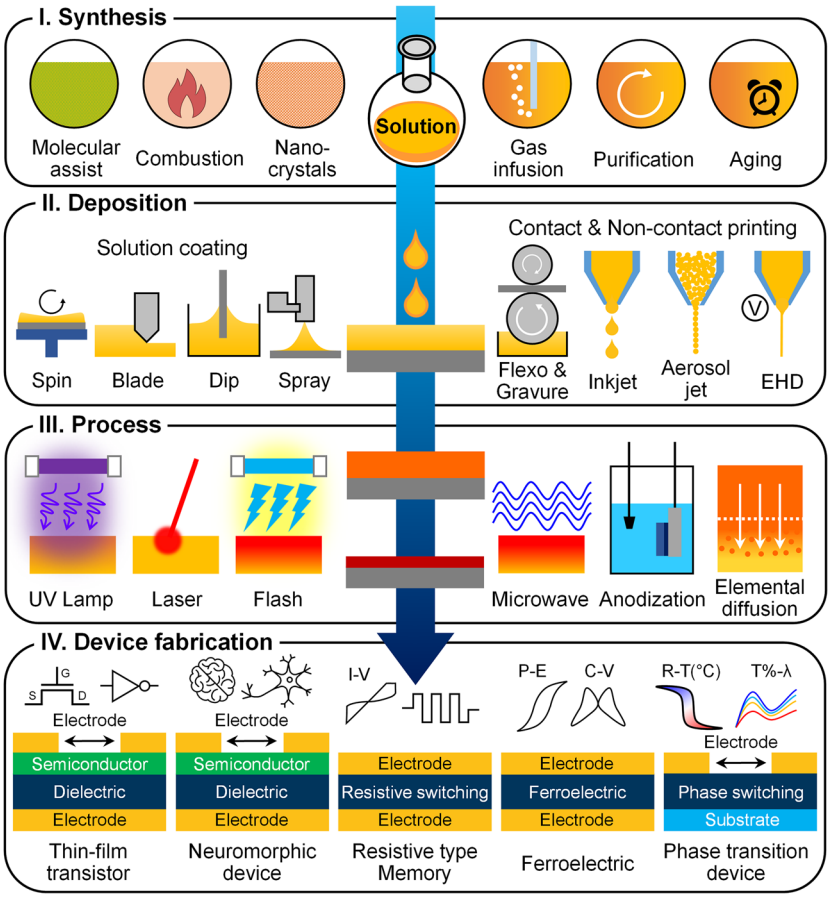

FIG. 1. Scheme of the solution-processed metal oxide dielectric films showing four steps (I–IV) for the two classes of electronic application: (I) synthesis design of dielectric precursor solution, (II) solution deposition methods based on both contact-printing and noncontact-printing, (III) film formation process, and (IV) device fabrication of five types of functional devices (e.g., thin-film transistor, neuromorphic device, resistive-type memory, ferroelectric device, and phase transition device).

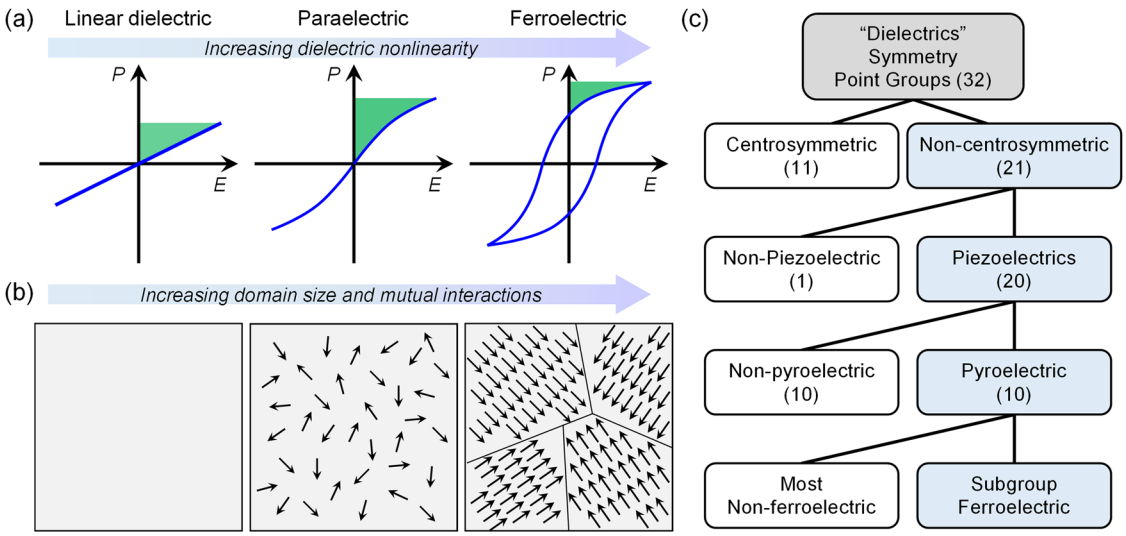

FIG. 2. A typical dependence of (a) polarization as a function of the electric field and (b) domain structures and dipole interactions for linear dielectric, paraelectric, and ferroelectric materials. (c) Interrelationship among different crystal point groups of dielectric materials.

molecules, ions, and defects. Piezoelectric materials can accumulate electric charges in response to the applied mechanical stress. Typically, the linear electromechanical interaction can be observed in the piezoelectric effect. Pyroelectric materials are a group of piezoelectrics that exhibit polarization changes in response to temperature changes. As a subgroup of pyroelectrics, ferroelectric materials exhibit a spontaneous net electric dipole moment. Their cooperative coupling of ferroelectric domains enables remnant electric polarization when the external E-field is zero and the P–E curve shows hysteresis. Generally, materials exhibit ferroelectric behaviors only below the phase transition temperature, called Curie temperature (T_c), and lose their pyroelectric properties. Above this temperature, many ferroelectric materials transform into the paraelectric state because their crystals undergo structural phase transition. The typical P–E behaviors and their domain structures of linear dielectric, paraelectric, and ferroelectric materials are displayed in Figs. 2(a) and 2(b), respectively.

According to Neumann's principle,[19–21] the symmetry of materials, including dielectric permittivity, elastic compliance, and electrostriction, can strongly influence the polarization properties of dielectrics. In view of the 32-crystal point group [Fig. 2(c)], piezoelectric and other effects belong to 20 noncentrosymmetric point groups because odd-rank tensors are forbidden in the centrosymmetric point group. Among these 20 piezoelectric point groups, half exhibited a spontaneous polarization effect in the absence of an external electric field. In addition to the crystalline structure at the atomic level, the alignment of electric dipoles in the long-range order (domain characteristics) is also an important factor in ferroelectrics. The typical polarization behavior of dipolar and ferroelectric domain structures with mutual interactions (e.g., dipole–dipole and domain–domain) is schematically illustrated in Fig. 2(b). Although these different dielectric materials have distinct functionalities, each has its own advantages with regard to electronic device applications.

For the electrical functionality of sol-gel dielectrics, it is necessary to produce oxide films with minimal defects and smooth surface morphology for stable electrical insulation with frequency-dependent capacitance performances. A facile chemical design, deposition, and post-treatment to control the amorphous/crystalline structure promote high-performance, excellent reliability, and new multifunctionalities.[4] Additionally, low-temperature and rapid fabrication methods to realize the high-throughput [roll-to-roll (R2R), sheet-to-sheet (S2S), etc.] printing process should be further studied. Figure 3 exhibits the research trends on the solution-processed oxide dielectric films and their application to functional electronic devices reported between 2015 and 2020 based on the extensive search on Web-of-Science. Overall, the number of research publications and citations of the solution-processed oxide dielectric films has continuously increased every year. Notwithstanding the growing research interest in solution-processed oxide dielectric films, recent research reviews have addressed mainly specific applications of solution-processed oxide dielectric films. Therefore, there exist few reviews that comprehensively encompass the developments of various functional oxide materials and enlargement of research fields for solution-processed oxide dielectric films and address the mainstream of the technological progress and trends as a broad outlook.

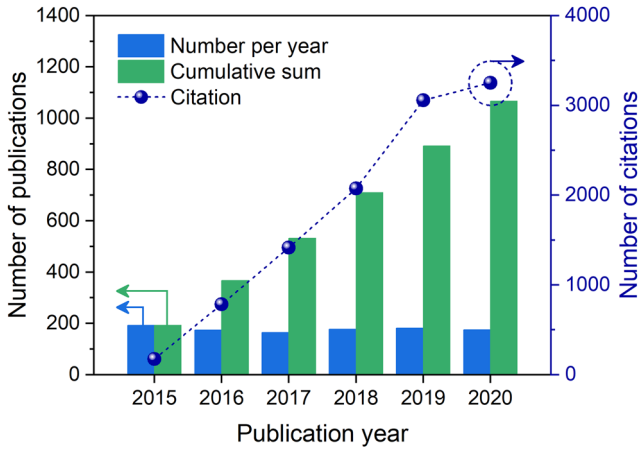

FIG. 3. The statistical analysis of the research trends with the number of the research publications and citations about the solution-processed oxide dielectric films and their application to functional electronic devices reported between 2015 and 2020 based on the extensive search on Web-of-Science with the detailed search conditions.

In this regard, we review recent research progress on solution-processed metal oxide dielectrics and their various electronic device applications from a literature survey over the past five years: (i) *three-terminal-based devices* such as a gate dielectric layer for a field-effect transistor (Sec. II) and (ii) *two-terminal-based devices* such as memory devices, including the types of resistive switching behaviors (Sec. III), ferroelectric functionalities (Sec. IV), and phase transition behaviors (Sec. V) (Fig. 1). While there have been many recent reviews on sol-gel metal oxide semiconducting materials in the application of thin-film-transistors, including the *p*-type active layer,[22,23] chemical solution synthesis,[4,24–26] low-temperature processing,[7,27–29] and miscellaneous device applications,[16,30–32] here, we aim at reviewing ongoing and future research development in solution-derived metal oxide dielectric thin films by (1) providing fundamental insights into the mechanism of sol-gel chemistry and (2) facilitating their practical application and commercialization in many fields of electronic and energy technology, such as complementary metal oxide semiconductor (CMOS) integrated logic circuits, sensors, and energy storage/conversion devices.

II. THIN-FILM TRANSISTORS

Over the past few decades, solution-processed high-quality metal oxide dielectric materials have been extensively researched for large-scale electronic applications (such as TFTs, sensors, and wearable devices) owing to their good electrical properties, good film uniformity with reliable electrical performance, environmental/chemical stability, and cost efficiency.[4–6] Silicon dioxide (SiO_2), as a common and reliable dielectric oxide, is used to date. However, with increasing demands for higher integrity of the complex circuit design with corresponding high performance, drastically downscaling the switching transistor has been challenging, concurrent with the significant reduction in dielectric thickness.

The SiO_2 layer with atomic-scale thickness has serious problems, such as a high leakage current density and poor device reliability.[4,5] In accordance with the capacitance equation, $C = k\varepsilon_0 A/d$ [where ε_0 is the permittivity of a vacuum, k is the dielectric constant or relative permittivity (ε_r), A is the area of parallel metallic plates, and d is the dielectric film thickness]. The use of the high-k ($k > 3.9$) dielectric layers is critical in preserving strong capacitive coupling[4–6] and suppressing tunneling effects (i.e., leakage current) compared to a typical thicker SiO_2 layer,[5,7] allowing for enhanced performance while lowering the power consumption (i.e., operating voltage) and device miniaturization. We categorized the manufacture of high-quality metal oxide dielectrics for TFT applications as follows: (1) preparation of sol-gel precursor solutions, (2) chemical solution deposition techniques, (3) post-deposition process at low temperature, and (4) large-scale and high-throughput manufacturing processes. Additionally, we introduce solution-processed neuromorphic devices employing oxide dielectrics as an emerging electronic application. Following our previously reported progress review,[4] we present the most recent research trends and technological advances of solution-processed oxide dielectrics for TFT devices reported since 2017 (cf. additional key reviews[5,7,27,33] of solution-processed oxide dielectrics for TFT devices with detailed basic mechanisms and historical movements in the past several decades). A summarized overview of the electrical performance of metal oxide TFT devices using sol-gel metal oxide dielectric layers is presented in Table I.

A. Synthesis of sol-gel precursor solution

1. Chemical doping and use of additives

The synthesis of precursor solutions is essential because the quality of the desired oxide films is influenced by sequential chemical reactions to form the M–O–M network. The acidity control of the precursor solution, for example, can improve the solubility of precursors and the hydrolysis reaction. Lee *et al.* reported the effect of solution acidity with H_2O_2 as an oxidizer to fabricate a $LaZrO_x$ (LZO) dielectric layer and TFT application.[34] As shown in Fig. 4(a), oxidant-assisted LZO films exhibit stirring temperature (T_s)-independent thermogravimetric behavior, whereas oxidant-free LZO films exhibited slow condensation at lower T_s. It was also proved that oxidative H_2O_2 can eliminate carbon residues using oxygen radicals during the deep ultraviolet (DUV) photochemical annealing process. They demonstrated that the LZO dielectric layer exhibits a low leakage current of 10^{-8} A/cm^2 at 2 MV/cm and a high breakdown E-field of 5.8 MV/cm, resulting in the high dielectric permittivity of 12 [Fig. 4(b)].

In addition to acidity control, anion doping in the precursor solution can improve the dielectric stability under a large window of frequencies. Zhuang *et al.* demonstrated fluoride (F) doping in AlO_x dielectrics by introducing an F-involving small molecule, 1,1,1-trifluoro-2,4-pentanedione, to overcome the frequency-dependent capacitance characteristics, yielding reliable film formation and stable device performance.[35] As shown in Fig. 4(c), such F sources were added to each precursor solution, and spin-cast F:AlOx films were repeatedly deposited to obtain the desired thickness. It was found that the optimized AlO_x dielectrics with an F content as high as 3.7 at. % exhibited a stable capacitance of 166 nF/cm^2 in the frequency range of 10^{-1}–10^4 Hz [Fig. 4(d)]. TFT devices using both inorganic and organic semiconductors exhibit negligible I–V hysteresis owing to the reduction in the H^+ content. These types of chemical approaches in solution synthesis fail to produce high-quality and low hysteresis of TFTs.

2. Chemical solution combustion synthesis (SCS)

Solution combustion synthesis (SCS) is an energy-efficient method that utilizes an exothermic reaction between fuels (reducing agents) and oxidizers (oxidizing agents) in a liquid metal-organic chemical supplying localized thermal energy to lower the processing temperature. Functional oxide materials and various structures (e.g., size and shape) with higher quality than those fabricated by conventional annealing processes have been reported.[36] Since Kim *et al.* published the first study on the device fabrication using metal oxide films via SCS with combustible precursors in 2011,[37] numerous studies on various applications of thin films have been conducted. Recently, various combinations of fuels and oxidizers comprising SCS have been actively studied, with new fuels, in particular, receiving widespread attention. Representative conventional combustion fuels [e.g., urea (U), acetylacetone (AcAcH), and hydrazine] and various acidic fuels [e.g., citric acid (CA), ethylenediamine tetra-acetic acid (EDTA), oxalic acid, oleic acid, tartaric acid (TA), and malic acid (MA)] have been studied.[24,26]

Chen *et al.* introduced a cofuel-assisted solution-combustion method that effectively lowers the general ignition temperature of the combustion process and encourages rapid completion of the combustion reactions.[38–40] Along with 3-nitroacetylacetone (NAcAcH),[38] other carbohydrate-based cofuels include ethylene glycol ($C_2H_6O_2$), erythritol ($C_4H_{10}O_4$), xylitol ($C_6H_{12}O_5$), glucose ($C_6H_{12}O_6$), sorbitol ($C_6H_{14}O_6$), sucrose ($C_{12}H_{22}O_{11}$), and *L*-ascorbic acid ($C_6H_8O_6$) (vitamin C).[39] However, they mainly applied to oxide semiconductors (IZO, IGZO, In_2O_3, etc.). Their recent study applied both semiconductors and dielectric films using a fluorinated cofuel (FAcAcH, 1,1,1-trifuloroacetylacetone) (Fig. 5).[40] In the initial pre-annealing stage with a temperature of 120 °C, the ultrafast reaction and M–O–M lattice condensation are achieved within a short time of only 10–60 s for the film formation of aluminum oxide dielectrics. As a result, IGZO/Al_2O_3 TFTs fabricated through a 60 s cofuel-assisted combustion processing have field-effect mobility as high as 25 cm^2/V s and stable operational performance even under a bias stress of 4000 s [Figs. 5(e) and 5(f)]. Combining with a blade-coating process, the wafer-scale TFTs—over 100 device units—have demonstrated reliable and high-quality device performance with average mobilities of 18 cm^2/V s [Figs. 5(b)–5(d)]. Parallel with the SCS process, it was proved that such systems can be applied as an efficient and continuous additive manufacturing to R2R.[40]

3. Cluster synthesis molecular-based precursor routes

The synthetic process incorporating a reducer and an oxidizer includes fastidious steps in terms of balancing the equivalence ratio. Nonstoichiometric combustion processes in the case of both fuel-rich and fuel-lean conditions could lead to large evolution

TABLE I. Parameters of thin-film transistor devices using the sol-gel metal oxide gate dielectric layer. [T_p: maximum processing temperature, Aq.: solution synthesis in an aqueous-based solvent (e.g., water), NonAq.: solution synthesis in a nonaqueous solvent, ED: elemental diffusion route, EHD: electrohydrodynamic printing method, SCS: solution combustion synthesis, DUV: deep-UV photochemical route, ELA: excimer laser annealing, SAND: self-assembled nanodielectric layer, PAD: polymer-assisted deposition, MW: microwave annealing, ML: molecular-based precursor synthesis route, IJ: inkjet printing, BL: blade coating, H_2O_2: additive loading of hydrogen peroxide, TPS: thermally purified solution process, SONO: sonochemical derived nano-dispersion methods assisted by ultrasound treatment, CRS: comproportionation reaction synthesis, ODS: oxygen-doped precursor solution synthesis, SVT: solvothermal treatment for cluster precursor synthesis, XF: xenon flash lamp photonic sintering, FL: flexographic printing method, μ: mobility of TFTs here (e.g., linear/saturation/field-effect), V_T: threshold voltage, *S.S*: subthreshold-swing, and $I_{ON/OFF}$: on/off current ratio of TFTs.]

							TFT performance				
Year	Material	Deposition	T_p (°C)	C_i(nF/cm^2)	Dielectric constant (k)	Processing feature	Channel material	μ_{sat} (cm^2/V s)	V_T (V)	*S.S.* (mV/dec)	$I_{ON/OFF}$
					Group Al_2O_3						
2017[45]	Al_2O_3	SC	60	~155	8.37	DUV ML	IGZO	3.61	2.58	196	>10^7
2018[58]	Al_2O_3/ZrO_2	SC	*130–180	···	8.53	DUV	IGZO	13.5	···	···	>10^7
2018[59]	AlO_x	IJ	<250	···	6~8	DUV	InO_x	~12	···	<150	>10^7
2018[68]	$Al_{0.45}Y_{1.55}O_3$	SC	400	443	19.5	···	IZO	52.9	−0.51	190	4×10^6
2018[69]	$La:Al_2O_3$	SC	350	96.1	10.5	···	IZO	11.9	···	380	~10^5
2018[70]	Al_2O_3	SC	250	~100	7.7	Aq.	In_2O_3	···	···	···	···
2018[71]	AlO_x	SC	250	560	~9	Aq.	InO_x	~52	···	···	~10^6
2019[72]	$Y:AlO_x$	SC	200	200	8.8	Aq.	IGZO	25.1	1.35	170	3.2×10^7
2019[40]	Al_2O_3	BL	350	286	6.8	SCS	IGZO	25.2	0.55	150	4×10^4
2019[73]	Al_2O_3	SC	200	74.1	~6	DUV MW	IGZO	1.23	···	120	5×10^4
2019[60]	$Y:AlO_x$	IJ	150	···	~8.8	DUV	IGZO	4.3	−0.5	300	10^8
2019[52]	Al_2O_3	EHD	350	···	···	SCS	In_2O_3	117.2	−0.41	95	>10^5
							IGZO	81.01	−0.15	81	
2019[54]	$Mg:AlO_x$	SC	180	148	···	ED	$Mg:InO_x$	>4	2.53	210	>10^7
2019[42]	Al_xO_y	SC	350	259	17.2	SCS ML	···	···	···	···	···
2019[43]	Al_xO_y	SC	350	86	11.8	SCS ML	IZO	7.1	8.7	···	1.4×10^5
2020[61]	$Y:AlO_x$	IJ	200	295	~10	DUV	IZO	15.6	···	<100	~10^8
2020[44]	$Y:Al_xO_y$	SC	150	~29	~6.4	DUV ML	IZO	2.6	12.4	···	1.8×10^7
2020[74]	AlO_x	SC	150	450		DUV SCS	$MAPbI_3$	11.5	−0.21	120	~10^4
2020[66]	AlO_x	FL	180	~300	8.2	DUV SCS	In_2O_3	2.83	···	~80	~10^6
2020[75]	AlO_x	SC	800	97	···	···	$NdAlO_3$	9.93	−5.22	···	~10^6
2021[53]	Al_2O_3	EHD	400	···	···	ED	Al:ITO	6.46	1.78	0.42	7.5×10^7
2020[67]	AlO_x	SC	150	420	9	SCS ELA	IGZO	20.4	~0	100	~10^4
2020[35]	$F:AlO_x$	SC	300	166	4	···	In_2O_3	12.8	~0	200	~10^4
2020[76]	AlO_x	SC	85	180	8.3	DUV	C10-DNTT	1.8	−0.72	110	4×10^5
2020[77]	AlO_x	SC	300	140	10.3-	Aq.CRS	In_2O_3	129	−0.4	170	~10^5
2021[55]	$Mg:AlO_x$	SC	180	~130	···	ED	$Mg:InO_x$	4.72	···	···	1.8×10^6
	$Hf:AlO_x$	$Hf:InO_x$	2.83	2.9×10^4							
2021[64]	$AlOx/AlSiO_x$	SC	150	380	···	DUV	IGZO	~0.3	0.09	51.1	>10^4

TABLE I. (*Continued.*)

Year	Material	Deposition	T_p (°C)	C_i(nF/cm^2)	Dielectric constant (k)	Processing feature	TFT performance: Channel material	μ_{sat} (cm^2/V s)	V_T (V)	S.S. (mV/dec)	$I_{ON/OFF}$
					Group ZrO_2						
2018[78]	ZrO_2	SC	300	⋯	~10	Non-aq.	Pentacene	3.7	−2.7	650	1.1×10^6
2018[79]	Gd:ZrO_2	SC	400	531	⋯	Aq. DUV	In_2O_3	18.82	1.04	80	~10^7
2019[80]	ZrO_2	SC	230	270	14.1		In_2O_3	19.4	0.58	90	~10^6
2020[81]	ZrO_x	SC	220	558	~6	SAND	Pentacene	0.36	−1.46	⋯	~10^4
2020[82]	ZrO_2	SC	400	160	19		IGZO	2.5	−0.13	550	6.2×10^5
2020[83]	ZrO_2	SC	57.5	446	8.2	DUV SAND	In_2O_3	26.21	0.29	125	3.9×10^3
2020[84]	ZrO_2	SC	150	~20	5.17		IGTO	21.7	~5.9	680	2.0×10^7
2020[62]	ZrO_2/Al_2O_3	SC	<200	~120	⋯	XF	ZnO/In_2O_3	2.3	0.86	123	>10^5
2020[63]	ZrO_2	SC	<200	~200	~7.5	XF	⋯	⋯	⋯	⋯	⋯
2020[85]	ZrO_x	SC	90	260	22	DUV	IZO	8.2	0.2	130	~10^5
2020[86]	LZO	SC	350	⋯	16	SONO	IGZO	5.45	−2.1	⋯	~10^5
2021[34]	LZO	SC	180	233	13.1	DUV H_2O_2	IGO	24.7	0.14	160	10^6
2021[87]	ZrO_2	SC	350	-	19.5	ODS	In_2O_3	60.42	0.32	140	~10^6
					Other oxides						
2017[88]	Yb_2O_3	SC	500	352.8	11.3		In_2O_3	4.98	0	70	~10^6
2017[65]	HfOx/HfOx	SC	150	328	9.8	SCS DUV	IGZO	43.9	⋯	66	10^6
2018[50]	HfO_x	SC	200	140	10.23	TPS	In_2O_3	3.67		180	9.8×10^6
2019[42]	Y_xO_y	SC	350	84	14.9	SCS ML	IZO	2.1	6.9	⋯	7.6×10^5
2019[47]	GaO_x	SC	500	178	10.8	PAD	In_2O_3	3.09	0.83	180	1.8×10^5
2019[48]	Al:HfO_2	SC	400	674	30.2	PAD	⋯	⋯	⋯	⋯	⋯
2020[49]	LaO_x	SC	120	⋯	>12	ODS	Pentacene	0.37	−0.59	⋯	3×10^5

of gases, resulting in highly porous morphology.[41] To avoid such phenomena, Koslowski *et al.* demonstrated a molecular single-source precursor approach using newly designed molecules to have both the roles of fuel and oxidizer.[42–44] They synthesized nitrofunctionalized malonato complexes, shown in Fig. 6(a), and used them to fabricate Y_xO_y dielectrics. They controlled the thermal conversion of the precursor at temperatures between 250 and 350 °C for an in-depth investigation of the formation of volatile by-products and for the optimization of relatively lower decomposition temperatures from the combustion reaction. The synthesized molecular precursor, bis(diethyl-2-nitromalonato) nitrato yttrium (III) (Y-DEM-NO_2), exhibited a frequency-independent capacitance of up to 250 nF/cm^2 [Fig. 6(b)] and stable insulating properties ($J \sim 1.0 \times 10^{-9}$ A/cm^2 at 1 MV/cm). This study suggested a potential alternative of the cost-effective synthetic route for low-temperature high-k dielectric materials.

In a similar but more innovative approach, Jo *et al.* synthesized bulky metal–oxo–hydroxyl nanoclusters [Fig. 6(c)] with few impurities and combined them with a spatially controllable and highly energetic light activation process, resulting in the highly reliable aluminum oxide at low process temperatures.[45] It has also been demonstrated that solution-based dielectric films can be directly fabricated on flexible polymeric and stretchable substrates. It was shown that the metal–oxo–hydroxy cluster-based thin film coated with light activation not only effectively decomposes but also forms a robust atomic network at low temperature and has a high breakdown electric field (>6 MV/cm), low leakage current density (~1 × 10^{-8} A/cm^2 at 2 MV/cm), and excellent electrical stability [Fig. 6(d)]. The recent updates in the fabrication of low-temperature metal oxide films through photochemical activation will be covered in more detail in later chapters.

4. Polymer-assisted deposition (PAD)

Although the aforementioned groups demonstrated a molecular-based precursor route, the incorporation of polymers such as polyethylenimine (PEI) into the precursor solution has been in progress recently, which is called polymer-assisted

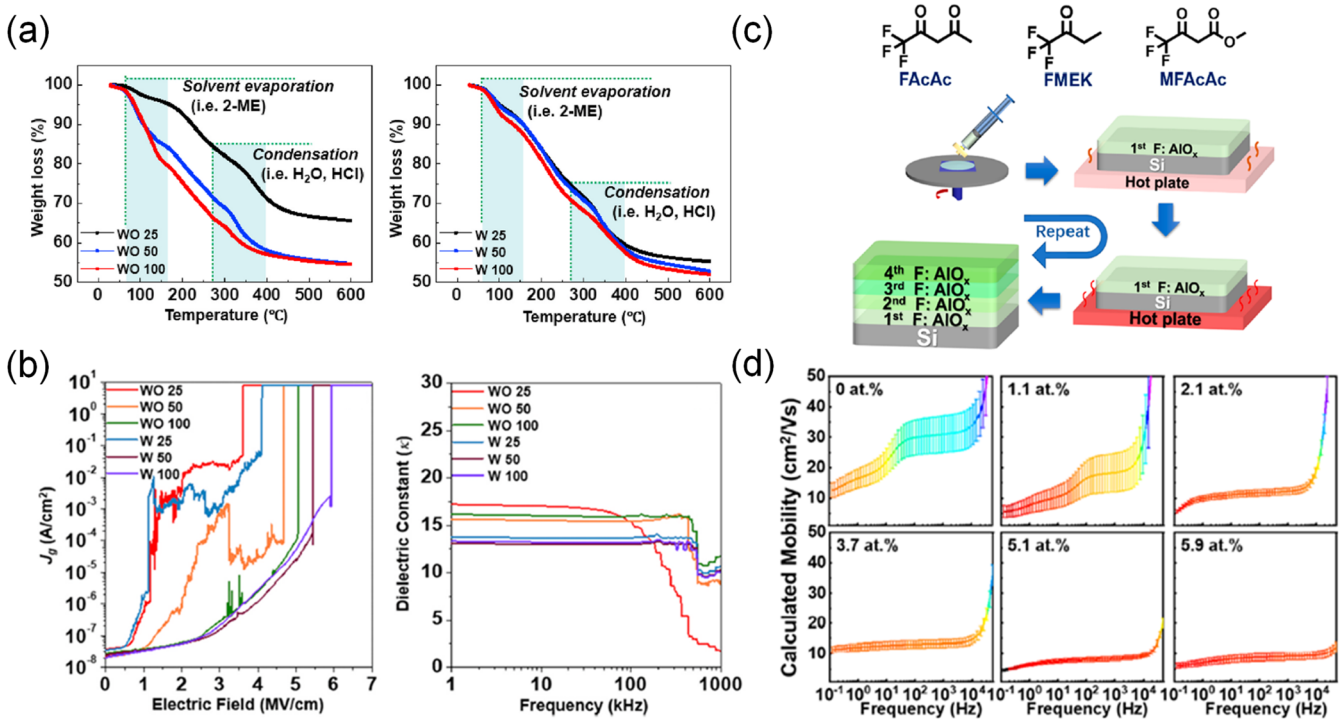

FIG. 4. (a) Thermogravimetric analysis (TGA) and (b) dielectric characteristics of (WO-25, 50, 100) oxidant-free and (W-25, 50, 100) oxidant-assisted LZO films at each different stirring temperature (T_S) from 25 to 100 °C. Reproduced with permission from Lee *et al.*, Ceram. Int. **47**, 6918 (2021). Copyright 2020 Elsevier. (c) Chemical structure of F-involving molecules: 1,1,1-trifluoro-2-butanone (FMEK), methyl 4,4,4-trifluoroacetoacetate (MFAcAc), and 1,1,1-trifluoro-2,4-pentanedione (FAcAc) and schematic of the fabrication of the F:AlO_x dielectric film. (d) Frequency dependency of mobility according to each different concentration of the incorporated F atoms. Reproduced with permission from Zhuang *et al.*, J. Am. Chem. Soc. **142**, 12440 (2020). Copyright 2020 American Chemical Society.

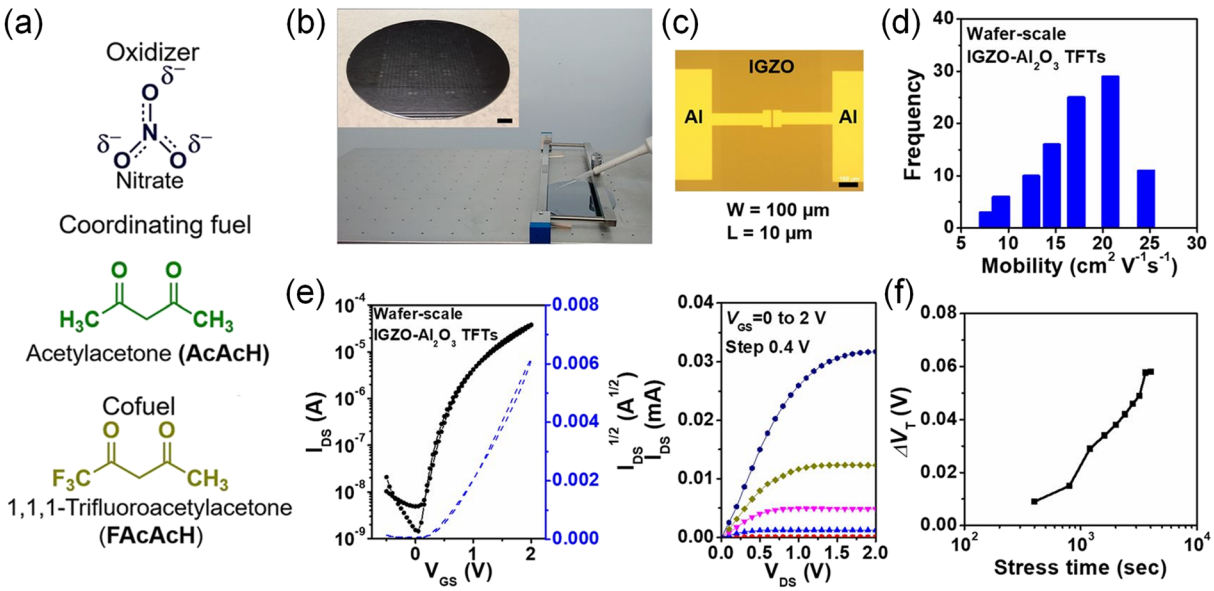

FIG. 5. (a) Chemical structures of nitrates (as an oxidizer), acetylacetone (AcAcH, as a coordinating fuel), and 1,1,1-trifluoroacetylacetone (FAcAcH, as a cofuel) for efficient solution combustion synthetic reactions. (b) Photo of the scalable combustion blade coating process (inset: blade-coated device array on a 4 in. silicon wafer). (c) Optical microimage of a patterned low-voltage IGZO/AlO_x TFT. (d) Statistical distribution of saturation mobilities of the large-scale fabricated device array. (e) Representative transfer and output curves of IGZO/Al_2O_3 TFTs under low-voltage operation. (f) V_T shift behavior of the fabricated device under bias stress time. Reproduced with permission from Wang *et al.*, Proc. Natl. Acad. Sci. U. S. A. **116**, 9230 (2019). Copyright 2019 National Academy of Sciences.

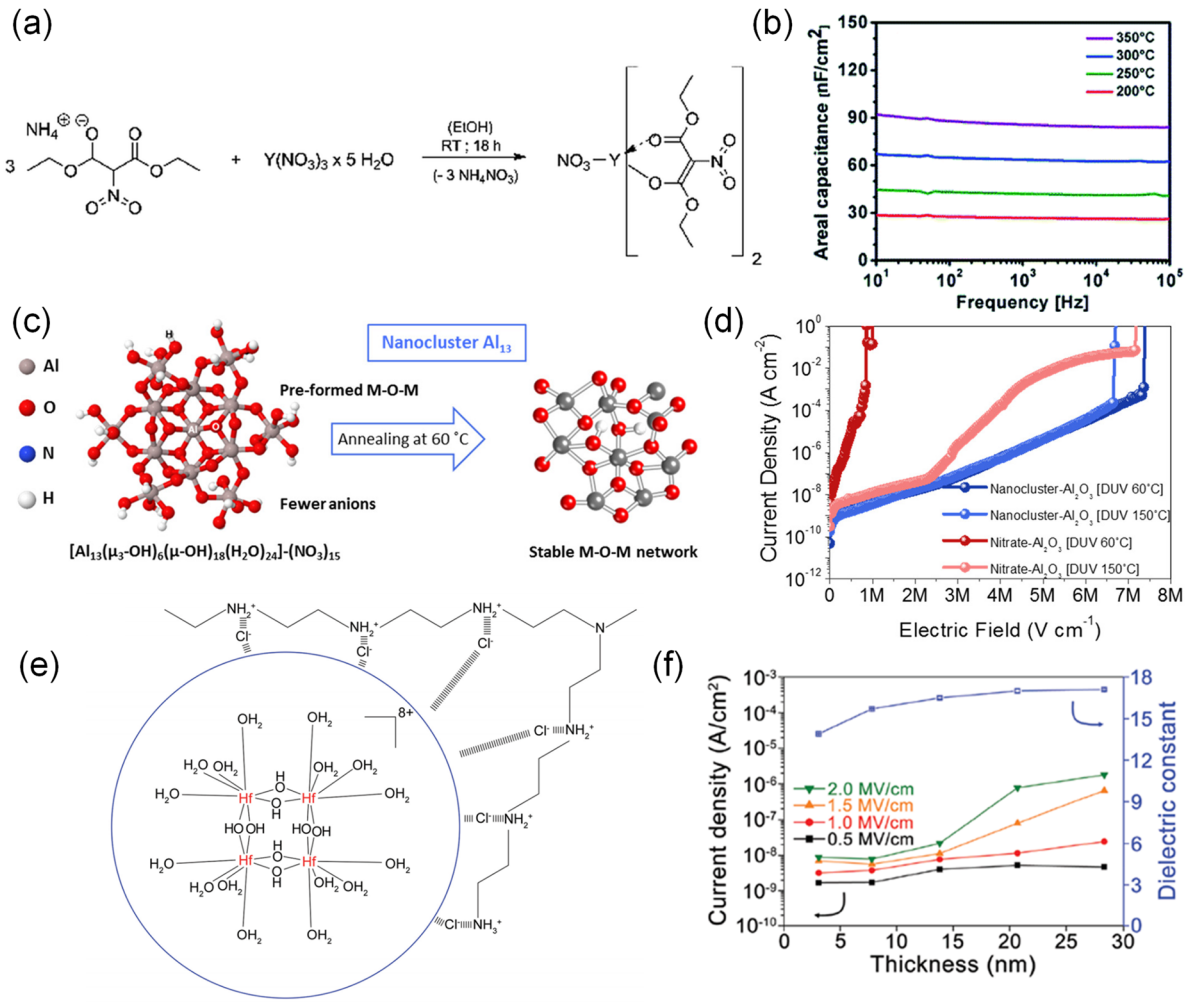

FIG. 6. (a) Schematic of the synthesis of bis(diethyl-2-nitromalonato) nitrato yttrium(III) (Y-DEM-NO_2) and the reaction scheme for the formation of metal urea compounds of yttrium. (b) Curves of areal capacitance vs frequency of solution-processed Y-DEM-NO_2 precursor dielectric layers at different annealing temperatures. Reproduced with permission from Koslowski *et al.*, RSC Adv. **9**, 31386 (2019). Copyright 2019 Royal Society of Chemistry. (c) Schematic of the synthesized nanocluster A13 precursor and alumna structure formed by the DUV photochemical route at 60 °C. (d) Plots of leakage current density (*J*) vs electric field for the alumina dielectric layers at different film preparation conditions. Reproduced with permission from Jo *et al.*, ACS Appl. Mater. Interfaces **9**, 35114 (2017). Copyright 2017 American Chemical Society. (e) Schematic illustration of the cationic Hf complex ion bound to the HCl from the amine groups of the PEI polymer. (f) Representative plots for the current density on the variation of the electric fields and the calculated dielectric constant depending on the film thickness. Reproduced with permission from Park *et al.*, Adv. Mater. Interfaces **6**, 1900588 (2019). Copyright 2019 John Wiley and Sons, Inc.

deposition (PAD) method.[46] In contrast to the conventional sol-gel reaction, which forms free-standing metal hydroxide (M-OH) via the hydrolysis reaction, such introduced polymers block the unwanted hydrolysis reaction through the formation of metal–ligand–polymer clusters until the polymers decompose above 600 °C, as shown in Figs. 6(e) and 6(f). The controlled chemical reaction causes the abrupt elimination of polymers at a critical temperature and results in a well-ordered oxide framework with a low density of defects in the amorphous state.

Chen *et al.* reported that GaO_x thin films using PAD exhibited superior dielectric performance before crystallization with the annealing temperature as high as 650 °C.[47] PAD-based GaO_x exhibited smooth morphology with a rms of 0.326 nm, an areal capacitance of 177 nF/cm^2 at 100 Hz, and a leakage current of 10^{-6} A/cm^2 at 1.5 MV/cm with a relatively high dielectric constant (k) of 10.8. Additionally, Park *et al.*[48] reported the effect of acidity in the PAD method on a hafnium oxide dielectric by controlling the additive HCl concentration, which demonstrated that the low pH helped to electrostatically bind metal–ligand complexes with PEI because of the large number of nitrogen atoms in PEI [Fig. 6(e)]. A large number of metal–ligand–PEI complexes stopped the unwanted hydrolysis reaction of Hf^{4+}, which could derive a well-defined HfO_2 framework by a controlled condensation reaction and the homogeneous distribution of the Al dopant by stable coordination.

PAD-based Al:HfO_2 has a dielectric constant value of 30.2 and a capacitance of 674 nF/cm^2 at 1.0 kHz [Fig. 6(f)].

5. Various solution treatments

Gas treatment during solution synthesis can also enhance the dielectric performance of oxide films. Yan *et al.*[49] investigated the incorporation of oxygen gas into a La_2O_3 sol-gel solution at different flow rates to improve the poor wettability of the precursor solution on the target substrate, as shown in Figs. 7(a) and 7(b). Increasing the flow rate of oxygen gas caused a color change in the solution with a decreasing contact angle caused by the generated hydroxide group. The La_2O_3 films with gas infusion treatment exhibited superior densification close to the oxide films using atomic layer deposition (ALD) with outstanding dielectric and insulating performances [Fig. 7(c)]. They proved that the gas treatment of a sol-gel solution was applicable for other oxide dielectrics.

Chung *et al.*[50] proposed a thermally purified solution (TPS) process in which applying thermal energy in solutions before film formation could be effective in fabricating a hafnium oxide framework. The detailed mechanism of this scheme is shown in Fig. 7(d). The TPS facilitated the hydrolysis reaction in the solution phase, which is called prehydrolysis, whereas a general hydrolysis reaction occurs after film casting. Because of the evaporation of by-products during prehydrolysis, the reaction required less thermal energy for the formation of the oxide framework. Conventionally synthesized HfO_x sol-gel solutions were heated at different temperatures from RT to 125 °C on a hot plate before spin-casting. The TPS-assisted HfO_x films annealed at 200 °C exhibited similar dielectric performance to the conventionally annealed films at 350 °C. The TPS-assisted HfO_x gate dielectric layer showed excellent electrical properties, such as a low leakage current density (~10^{-9} A/cm^2 at 2 MV/cm), a high breakdown electric field (6 MV/cm), resulting in good TFT device performance with a mobility of 3.67 cm^2/V s, and an on/off current ratio of over 10^6 [Figs. 7(e) and 7(f)].

B. Chemical solution deposition techniques

1. High-resolution solution printing and elemental diffusion approaches

As a newly developed noncontact jet printing technique,[51] electro-hydrodynamic (EHD) jet printing has been developed based on the electro-hydrodynamic effects of the electric field actuation between an ink nozzle and a conductive supporting substrate. It has many advantages, such as a high printing resolution (e.g., linewidth below 100 nm), a wide range of selection for printable inks (good ink compatibility with a viscosity of 1–1000 mPa s), and cost-effective use of materials [Fig. 8(a)]. Liang *et al.*[52] proposed a scalable approach for all-printed transparent metal oxide TFTs—a direct EHD jet printing process for high-resolution micropatterning in combination with solution combustion-derived metal oxide precursor inks, such as semiconducting [In_2O_3, In-Ga-Zn-O(IGZO)], conducting [Sn-doped In_2O_3 (ITO)], and gate dielectrics

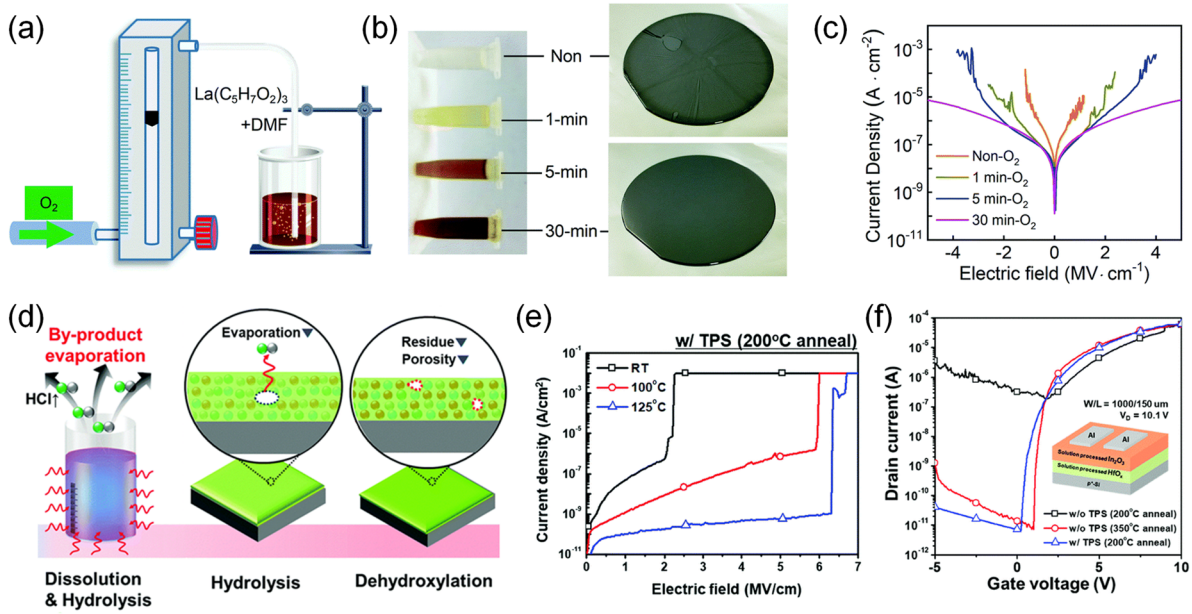

FIG. 7. (a) Schematic of the experimental setup for oxygen infusion into the lanthanum oxide precursor solution. (b) The photo-image of the precursor solution with various oxygen infusion times after 12 h stirring for reaction and as-spun films on silicon wafers. (c) *J–E* curves for insulating properties for the dielectric layers with different oxygen infusion times. Reproduced with permission from Yan *et al.*, J. Mater. Chem. C **8**, 5163 (2020). Copyright 2020 Royal Society of Chemistry. (d) Schematic illustration of the thermally purified solution process (TPS) to efficiently reduce the processing temperature of the HfO_x film. (e) *J–E* curves of the dielectric HfO_x films at different TPS temperatures with annealing temperature at 200 °C. (f) Transfer curves of In_2O_3 TFTs employed with HfO_x layers with and without the TPS process. Reproduced with permission from Chung *et al.*, J. Mater. Chem. C **6**, 4928 (2018). Copyright 2018 Royal Society of Chemistry.

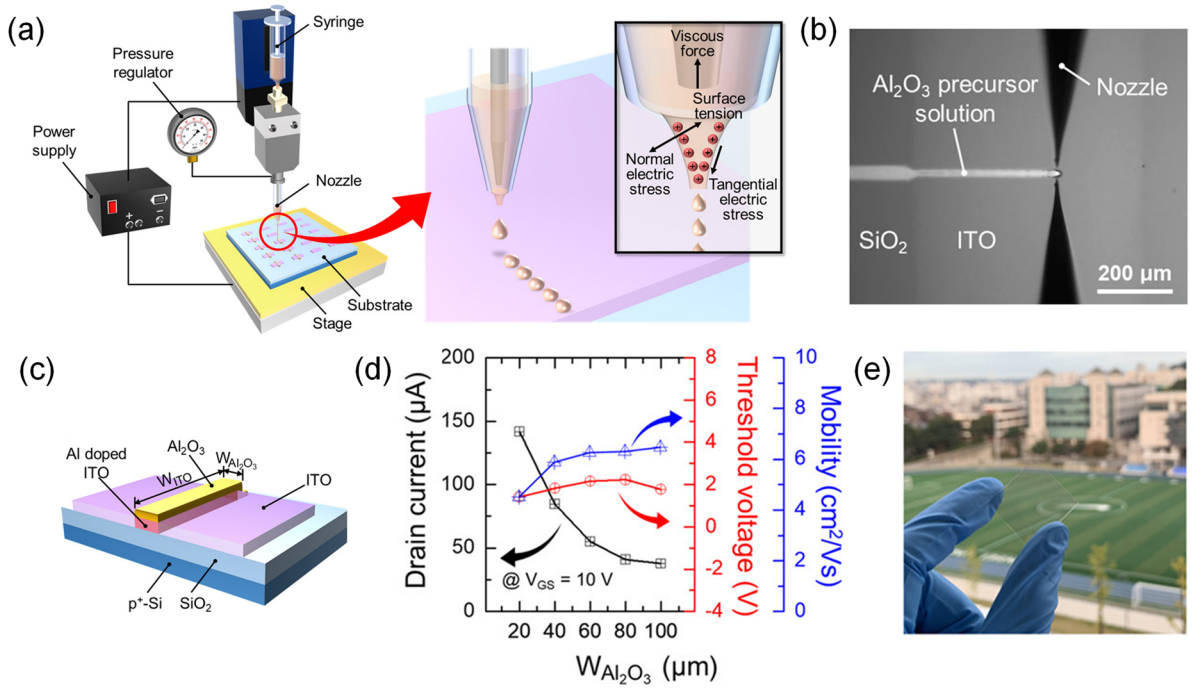

FIG. 8. (a) Schematic of the electrohydrodynamic (EHD) jet-printing system. (b) Photo-image of EHD jet printing of aluminum oxide precursor solution on the ITO film. (c) Schematic image of the fabricated homojunction-structured Al-doped ITO TFT devices with jet-printed dimensions of W_{AlOx} and W_{ITO}. (d) Drain current, threshold voltages, and field-effect mobility at V_G of 10 V from the homojunction-structured TFTs with varying W_{AlOx}. (e) Photo-image of the fabricated transparent NMOS inverter device. Reproduced with permission from Hong *et al.*, ACS Appl. Mater. Interfaces **12**, 39705 (2020). Copyright 2020 American Chemical Society.

(Al_2O_3). The fully printed oxide TFTs achieved a high electron mobility of 117 cm^2/V s with negligible hysteresis, excellent uniformity, and stable low-voltage device operation (2 V) due to high capacitance (~130 nF/cm^2 at 1.0 kHz) of aluminum oxide dielectrics. With elaborate and rapid device performance, they also demonstrated large-scale integrated logic gates, such as NOT and NAND.

Through the direct EHD jet printing of a solution of an Al_2O_3 dielectric layer with fine printed dimensions [such as linewidth (W) and length (L)] on a patterned ITO glass substrate, Hong *et al.*[53] reported a simple and novel fabrication method for homojunction-structured TFTs with an Al-doped ITO semiconductor on the printed Al_2O_3 dielectric layer (Fig. 8). The specific Al_2O_3-EHD-printed regions of the ITO film converted a conducting layer into a semiconducting channel layer (i.e., Al-ion-diffused ITO layer) with the simultaneous formation of a passivation layer through a thermal annealing process. The channel length and width of the fabricated TFT are determined only by the printed region of the Al_2O_3 layer, implying that this proposed method provides flexible device fabrication while using a minimum number of patterning masks. They fabricated transparent *n*-type metal–oxide–semiconductor (NMOS) TFTs and inverters, exhibiting a field-effect mobility of 6.45 cm^2/V s (W/L ~600/100) and an output voltage gain of 7.13 with a supply voltage of 10 V [W/L ~500/300 (load) and ~200/100 (drive)] via optimized processing conditions and Al_2O_3-printed dimensions [Figs. 8(c)–8(e)]. This is a promising approach compatible with a flexible manufacturing system for low-cost and mass production of high-quality metal oxide electronic devices.

Recently, research similar to the development of semiconducting properties of the Al-diffused ITO layer from printed Al_2O_3 has been conducted to obtain new electrical properties or enhanced performance by utilizing the interrelationship of elements between two different deposited metal oxide films during the annealing process. Heo *et al.*[54,55] reported a facile route to improve the film quality and interfacial properties of low-temperature solution-processed oxide thin films via elemental diffusion between metallic ion-doped indium oxide semiconducting layers and AlO_x gate dielectric layers. This approach provides the advantages of effective removal of residual impurities and suppression of oxygen vacancy defects and relevant dipole disorder in the AlO_x gate dielectric layer by metal–elemental doping using Mg or Hf (Fig. 9). They investigated the interfacial effects of various metallic dopants based on the metal ionic radius, metal–oxygen bonding-dissociation energies (BDEs), and Gibbs energies of oxidation reactions. In their first study,[54] they revealed that the AlO_x gate dielectric layer with moderate control of Mg-doping concentration (with optimal 10%) showed excellent operational stability because of the formation of a stable M–O–M network without any additional treatments. The Mg:InO_x TFTs based on the Mg-diffused AlO_x dielectric layer were performed using μ_{FE} > 4 cm^2/Vs, negligible hysteresis behavior, and stable device operation under the bias stability test. Afterward,

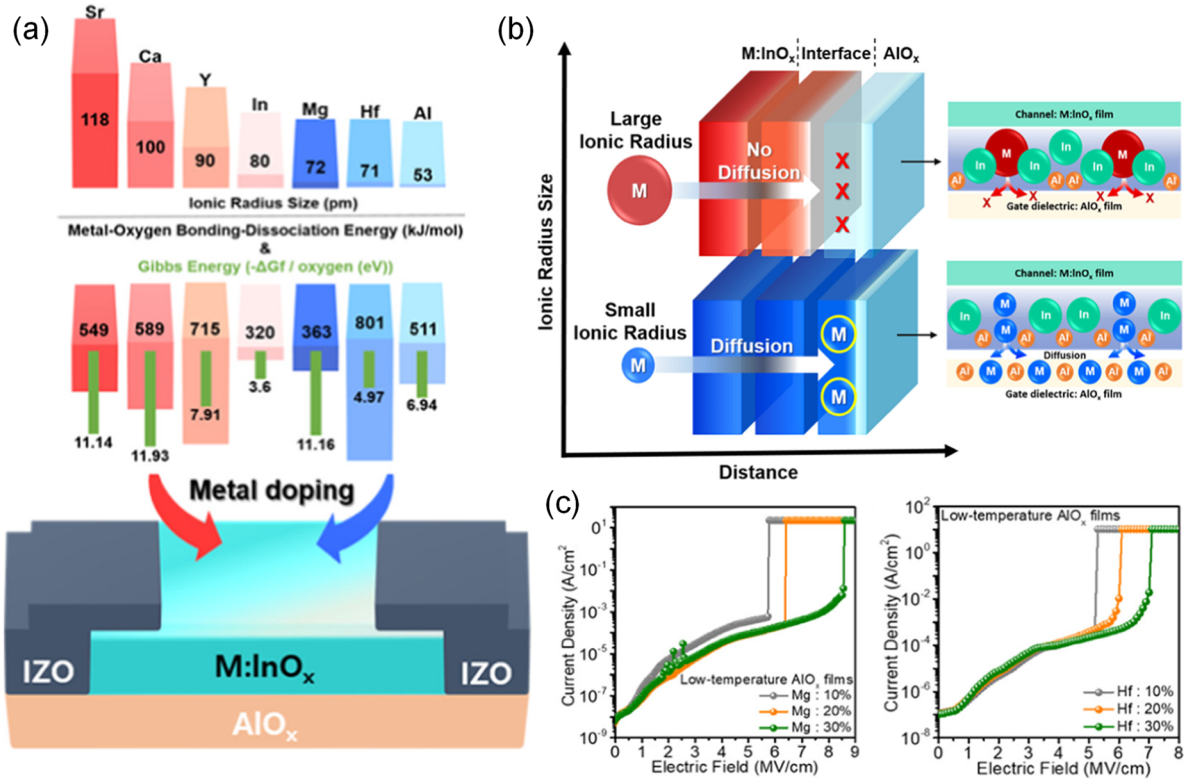

FIG. 9. (a) Schematic of the elemental diffusion process using various metal ions (Sr, Ca, Y, In, Mg, Hf, and Al) in the terms of ionic radius, metal–oxygen bonding dissociation energy (BDE), and Gibbs energy of oxidation for metallic dopants in the device structure of M:InO_x TFT on the AlO_x gate dielectric layer at low-processing temperature. (b) Scheme of metal ionic diffusion from an M:InO_x layer into the adjacent AlO_x dielectric layer according to the ionic radius of metallic dopants (M). (c) *J–E* curves of low-temperature solution-processed AlO_x dielectric layers inter-diffused with different adjacent M:InO_x channel layers. Reproduced with permission from Jeon *et al.*, ACS Appl. Mater. Interfaces **12**, 57996 (2020). Copyright 2020 American Chemical Society.

they demonstrated[55] that metallic dopants of Mg and Hf metallic dopants could diffuse into the low-quality AlO_x gate dielectric layer and diminish the structural defects and impurities in the bulk and at the interface between the semiconductor/dielectric layers because of their small ionic radii (less than 72 pm), high Gibbs energy of oxidation (in the case of Mg), and high BDE (in the case of Hf) [Figs. 9(a) and 9(b)]. Other dopants, such as Sr and Ca, which have a larger ionic radius than host metallic ions, deteriorate device performance and reliability because of the structural disorder and low diffusion rates at the interface between the semiconductor and dielectric layers [Fig. 9(c)]. As a result, the elemental diffusion approach, with metal dopants having a smaller ionic radius along with high BDE and Gibbs energy, offered prospective routes for improving the interfacial integrity of solution-processed metal oxide layers.

C. Low-temperature post-deposition process

1. Recent advances in UV photonic annealing for low-temperature process

Generally, the fabrication of a solution-processed oxide dielectric layer requires a high process temperature (over 400 °C) for high quality and desired performance. Many studies have been conducted to lower this temperature. The temperature is highly dependent on the amount of thermal energy required for converting the deposited films from the synthesized sol-gel solutions. Several studies[7,24,27,28] have been conducted to compensate for the required energy and/or to lower the activation energy barrier during the formation of metal oxide dielectric films using external energy resources. As the most representative method, the photonic annealing process via photoactivation through different variables [e.g., light source (laser/lamp), wavelength (UV to IR), irradiance and intensity, ambient gas, and irradiation time (continuous/pulsed)] not only drastically lowers the thermal energy for the formation of a M–O–M framework but also realizes that a high-quality metal oxide thin film can be fabricated on a flexible plastic substrate.

For the first time in 2012, Kim *et al.*[56] proposed DUV photochemical conversion of nitrate-based sol-gel precursors to fabricate metal oxide TFT devices based on amorphous oxide semiconductors (IGZO, IZO, and In_2O_3) at room temperature. They reported that DUV photochemical conversion (1) effectively removes organic impurities from the solution-deposited films, (2) induces photochemical cleavage to promote hydrolysis and condensation reactions, and (3) efficiently forms the M–O–M framework even

at low temperatures. In an in-depth follow-up study in 2015, Park *et al.*[57] reported the reaction mechanism of the DUV photochemical activation process of sol-gel metal oxide films, including various dielectric materials, such as AlO_x, ZrO_x, and HfO_x. Highly reactive radicals are generated from the photolysis of metal ligands (nitrate, acetylacetonate, and isopropoxide) under DUV photoactivation to remove organic impurities and rapidly promote film densification and polycondensation reactions. A decreasing tendency in the thickness of the as-spun films over time confirms the reaction. In 2018, Jo *et al.*[58] used the low-temperature photochemical activation method of an Al_2O_3/ZrO_2 bilayer gate dielectric oxide layer with high and stable performance (leakage current density ~10^{-9} A/cm^2 at 1 MV/cm, k ~ 8.53) and fabricated hysteresis-free solution-processed TFTs and seven-stage ring oscillators. Various gate dielectric thin film structures (e.g., single- and bi-layer and their different sequences) of Al_2O_3, ZrO_2, or sodium-doped Al_2O_3 materials were sequentially fabricated, and their performances and properties were compared. The physical mechanisms underlying its large hysteresis, low electrical performance, and instability in the electronic device operation have been investigated.

2. Technical integration of UV photonic annealing with solution-printing methodologies

To solve the challenges in integrating the UV-irradiation process and high-throughput multi-nozzle inkjet printing techniques, Scheideler *et al.*[59] demonstrated the fabrication of high-performance solution-printed InO_x TFTs with UV-annealed high-k AlO_x gate dielectric layers. Multi-nozzle printing in the design of AlO_x dielectric inks facilitated good film uniformity, rapid processing speed, and reduced processing time to 20 min. They addressed the influence of UV annealing on the formation of AlO_x gate dielectric layers and improved device reliability by bias-stress tests. They fabricated all-inkjet-printed oxide TFTs with all three layers, such as semiconductors, dielectrics, and source/drain electrodes, without additional vacuum processing and lithographic patterning, which otherwise impedes the fabrication throughput. The fabricated solution-processed InO_x transistors exhibited excellent device performance with high linear mobility (~12 cm^2/V s), negligible hysteresis, and a good subthreshold property at a low process temperature of 250 °C. Since then, many studies on inkjet-based high-k dielectric oxide films with UV-photonic annealing processes have been continuously conducted to decrease the processing temperature, which is compatible with temperature-sensitive flexible plastic substrates.[60,61]

D. Large-area and high-throughput manufacturing process

1. Advanced annealing processes for rapid fabrication

While it is essential to make solution-based oxide dielectric films of high quality and reliability, it is also important to introduce them to a continuous printing process (e.g., R2R and S2S) for high-throughput manufacturing of dielectric films within a short processing set time. In this regard, research has recently reported the rapid fabrication of oxide conductor/semiconductor/dielectric layers for fully printed electronic devices (1) by improving the existing methods and investigating unknown mechanisms or (2) by multiplying and combining various approaches (i + ii): (i) novel synthetic methods for improved oxide precursor solution systems, such as molecular doping,[34,35] SCS,[36–40] or nanocluster synthesis,[42–45] and (ii) efficient ways to supply the exterior energies and control environmental conditions of the deposited films, such as photonic irradiation,[56–61] or infusion of mixed gas type and pressure.[49,50]

Yarali *et al.*[62] presented the sequential solution-phase deposition of Al_2O_3/ZrO_2 and In_2O_3/ZnO bilayers and photonic processing using a short-pulsed xenon flash lamp (wide spectrum of 200–1100 nm, different energy densities, and simulated pulse length and number) to overcome two technical challenges: high process temperatures and lengthy annealing times [Fig. 10(a)]. The flash photonic processing in the ambient atmosphere provided a dramatic and temporal increase in the internal temperature of metal oxide precursor layers while minimizing the overall process time below 60 s without compromising the quality of the metal oxide layer. [Fig. 10(b)]. The fabricated Al_2O_3/ZrO_2 dielectric bilayers under the photothermally induced precursor conversion showed low leakage current density (10^{-6} A/cm^2 at 1 MV/cm), high areal capacitance (~120 nF/cm^2), resulting in high mobility (2.3 cm^2/V s), and low operation voltages (under 2 V) of TFTs with photonically converted In_2O_3/ZnO heterojunction semiconductor layers on a thermally sensitive flexible PEN (Polyethylene naphthalate) substrate [Fig. 10(c)].

Daunis *et al.*[63] also demonstrated high-speed photonic curing of solution-based high-k dielectric ZrO_2 layers on a flexible PEN substrate using a pulsed xenon flash system to resolve the two above-mentioned challenges (process temperature and time) for high-throughput processing and low-cost manufacturing. They reported that the curing and patterning processes were conducted concurrently using a self-aligned patterning method with a shadow mask for a photothermally induced precursor conversion of the oxide layer on top of patterned Al metal contacts. The fabricated ZrO_2 dielectric layer has a low leakage current density (~10^{-7} A/cm^2 at 2 MV/cm), high areal capacitance (200 nF/cm^2), low dissipation factor (0.03 at 100 kHz), and high breakdown field (~8 MV/cm from two ZrO_2 thin layers) with varied pulsed photonic conditions. They suggested that a photonic curing system under varied conditions [specification and input power of pulsed flash lamp and pulse number and rate (Hz)] can realize high-quality solution-deposited oxide dielectric films on flexible plastic substrates with a high oxide conversion rate to a high throughput beyond 30 m/min.

Recently, Lee *et al.*[64] demonstrated the rapid fabrication of a reliable sol-gel AlO_x dielectric bilayer through DUV photoactivation with low UV light intensity (~30 mW/cm^2) from a commercialized low-pressure mercury lamp. The correlation between the maximum process thickness and the concentration that can achieve the maximum efficiency of the DUV light activation process was revealed through optical analysis. Different types of high-quality metal oxide thin films were fabricated on a silicon substrate. In the fabrication of stable dielectric thin films, in addition to amorphous AlO_x, which is densified during DUV photoactivation, an $AlSiO_x$ (aluminum silicate) thin film—a stable oxide interface that can obtain effective dielectric polarization and minimum current leakage on the silicon substrate—can be formed for an exceptionally

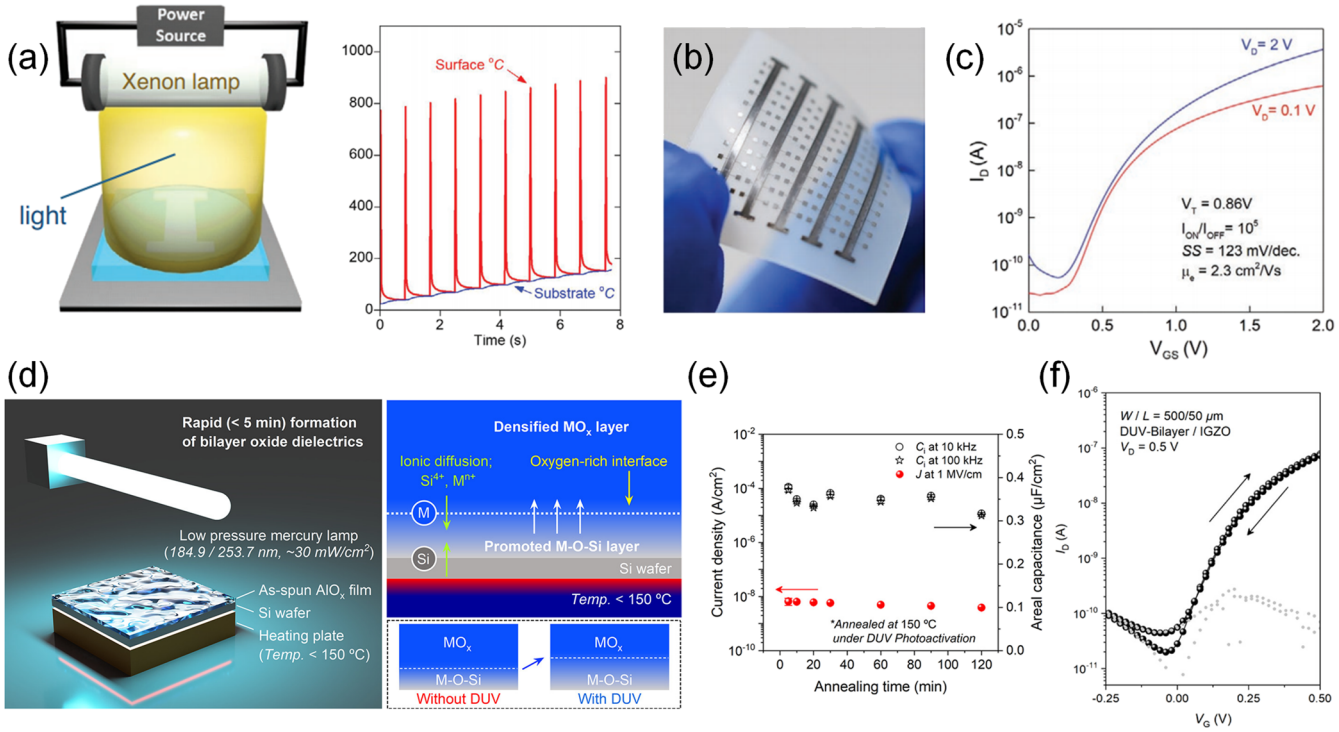

FIG. 10. (a) Schematic of the photonic curing process using high-intensity light pulses generated by a xenon lamp. The deposited precursor films on top of the Al electrode converted to the densified oxide layer after the light pulse exposures and the calculated temperature evolution on the surfaces of the final ZnO layer atop of the $In_2O_3/ZrO_2/Al_2O_3$/Al electrode/glass substrate using SimPulse software. (b) Photo-image of TFT arrays fabricated on a flexible PEN substrate. Its representative (c) transfer curves of In_2O_3/ZnO heterojunction-structured TFTs with Al_2O_3/ZrO_2 bilayer dielectrics. Reproduced with permission from Yarali *et al.*, Adv. Electron. Mater. **6**, 2000028 (2020). Copyright 2020 John Wiley and Sons, Inc. (d) Schematic of the rapid photoactivation process (below 5 min) for the fabrication of bilayer oxide (AlO_x-$AlSiO_x$) dielectrics on a silicon wafer substrate. (e) Statistical plots of J at 1 MV/cm and C_i in DUV-photoactivated bilayer dielectrics as a function of annealing time. (f) Double-sweep transfer curve of rapidly fabricated (5 min) IGZO and bilayer oxide dielectric TFT device under sub-0.5 V operating voltage. Reproduced with permission from Lee *et al.*, ACS Appl. Mater. Interfaces **13**, 2820 (2021). Copyright 2021 American Chemical Society.

short process time (within 5 min). Through various physicochemical and electrical characterization, they proposed a DUV photoactivation mechanism that allows aluminum atoms in AlO_x to be penetrated (e.g., ionic diffusion) into the silicon oxide layer [Fig. 10(d)]. As a result, the solution-processed oxide TFTs capable of sub-0.5 V operation were fabricated with only 5 min of processing time for each dielectric and semiconductor layer (IGZO) [Figs. 10(e) and 10(f)].

2. Combination studies for the low-temperature high-throughput processes

To overcome the challenge of poor productivity for the fabrication of uniform and condensed oxide dielectric layers on flexible plastic substrates, it is essential to lower the high process temperatures required to fully convert chemical precursor films to metal oxides. Carlos *et al.*[65] combined the urea-fuel-based SCS and UV lamp irradiation methods to fabricate single and multilayer films of high-k dielectric layers (AlO_x and HfO_x) that provide superior performance and quality at low temperature (150 °C). They synthesized a redox mixture under fuel-rich conditions to maximize the activation of the combustion reaction of AlO_x and HfO_x precursor solutions and to decrease the process temperature for metal oxide formation, ensuring that oxygen molecules are converted into fuel. Among UV photo-converted dielectric oxide multilayers, the HfO_x bilayer has the best electrical performance [low operation voltage (<3 V), high saturation mobility (~43.9 cm^2/Vs), and a good idle shelf-life stability (2 months)] when fabricated as TFT devices with the IGZO semiconductor. Furthermore, they employed their combined implementation in large-area AlO_x dielectrics on a flexible polyimide substrate using flexographic printing, which is an R2R-compatible and industrially scalable printing method [Fig. 11(a)].[66] They reported for the first time the large-area printing of highly stable ultrathin high-k AlO_x dielectric thin films using a high-throughput (50 m/min) onto a flexible substrate with a combined low-temperature annealing process (SCS + UV, below 200 °C). The fabricated AlO_x dielectric showed a low leakage current density (10^{-6} A/cm^2 at 1 MV/cm) with k ~ 8.2 (at 1 Hz). As shown in Fig. 11(b), the flexible TFT devices with the inkjet-printed In_2O_3 layer on the flexo-printed AlO_x layer achieved good electrical performance with enhanced operational stability with a negligible shift

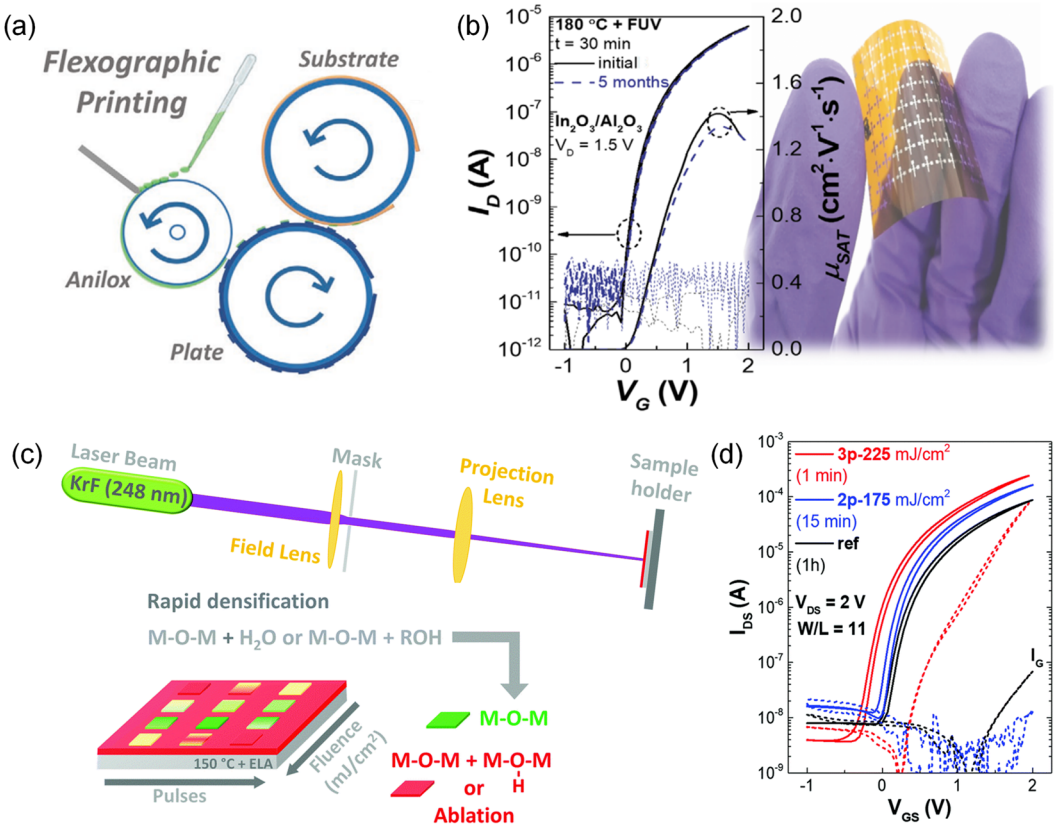

FIG. 11. (a) Schematic of the flexographic printing process of the SCS-based Al_2O_3 dielectric ink on top of the bottom electrodes deposited by thermal evaporation. (b) Transfer curves of initial and aged (over 5 months) In_2O_3 TFT devices with the Al_2O_3 dielectric layer through the subsequent printing processes (flexographic printing, UV photo-assisted annealing with SCS reaction, inkjet printing, and S/D electrode deposition by thermal evaporation). Reproduced with permission from Carlos *et al.*, Adv. Electron. Mater. **6**, 1901071 (2020). Copyright 2020 John Wiley and Sons, Inc. (c) Schematic illustration of the photonic annealing process with excimer laser for SCS-based AlO_x thin films with varying light fluences and the number of pulses, right after solution-film drying (i.e., soft-baking) with different times (15 or 1 min) at 150 °C. (d) Transfer curves of IGZO TFT devices with the laser-assisted AlO_x dielectric layers prepared with different light fluences and pulse numbers and drying times. Reproduced with permission from Carlos *et al.*, J. Mater. Chem. C **8**, 6176 (2020). Copyright 2020 Royal Society of Chemistry.

under electrical and mechanical stresses (e.g., aging effect, positive and negative bias, and continuous bending cycles).

They further implemented the fabrication of amorphous AlO_x thin films via solution combustion synthesis photo-triggered by excimer laser annealing (ELA from a 248 nm KrF pulsed excimer laser) for high-quality large-area oxide formation with a cost-efficient process with high throughput [Fig. 11(c)].[67] By combining ELA and SCS approaches, the fabricated AlO_x dielectric thin films achieved densification in a short process time—within 15 min—and a short drying cycle at 150 °C. They presented low surface roughness and optimized dielectric properties with low leakage currents (10^{-6} A/cm^2 at 1 MV/cm) and a high breakdown voltage (4 MV/cm) and dielectric constant ($k \sim 9$). The TFT devices for the fabricated AlO_x showed high saturation mobility ($\mu_{SAT} \sim 20.4$ cm^2/Vs) and a turn-on voltage close to 0 V [Fig. 11(d)]. This combination approach, with SCS and the subsequent ELA processing, will be significant to the high-throughput printed electronic industry.

E. Synaptic transistors for neuromorphic devices

Neuromorphic devices that mimic synaptic behavior using electronic devices have gained enormous attention owing to their low power consumption and rapid calculation with parallel operation.[89] For high-performance neuromorphic devices, the dielectric layer is key in controlling the operational voltage with minimized leakage current and polarization behavior under an applied E-field.[90] According to previous reports, most dielectric layers in neuromorphic devices are conventionally formed under a lengthy vacuum process accompanied by a high-temperature annealing process.[91] Therefore, for the further development of a cost-efficient process, it is necessary to secure a high-k sol-gel dielectric layer with proper electrical and polarization behavior. In this Research Update, we describe the electrical and capacitive behavior of sol-gel processed dielectric layers in neuromorphic devices and their fabrication approaches (cf. additional key review and the work of Liu *et al.*[16] for solution-based neuromorphic devices). The

TABLE II. Parameters of neuromorphic devices using the sol-gel metal oxide dielectric layer. (*: The parameter was calculated from the data in the reconstructed graph. PPF: pair pulse facilitation, STP: spike-timing-dependent plasticity, LTP: long-term plasticity, MSC: mesoporous silica, and SAO: sodium aluminum oxide.)

Year	Dielectric	Semi-conductor	Mobility (cm^2/V s)	$I_{ON/OFF}$	S.S. (mV/dec)	C_i (μF/cm^2)	Hysteresis window (V)	PPF (Δt)	STP	LTP
2016[92]	Sol-gel silica	IGZO	5.9	10^7	90	3.0	···	2.5 (20 ms)	✓	···
2019[93]	SAO	IGZO	6.5	$<10^7$	440*	3*	−3	1.28 (500 ms)	✓	✓
2020[94]	AlO_x	InO_x	1*	$<10^7$*	180*	3*	···	1.23 (10 ms)	✓	✓
2020[95]	AlO_x	LZO	···	$<10^9$	140*	···	···	>1.2	✓	✓
2021[96]	MSCs	ITO	1.3	3.0×10^6	122	2.8	−0.3	1.4 (10 ms)	✓	···

parameters of the neuromorphic devices described are summarized in Table II.

Shao *et al.* emulated the synaptic behavior with sol-gel-treated silica films with the deposition of two gate electrodes (G1 and G2) as lateral in-plane gate electrodes [Fig. 12(a)].[92] The silica film fabricated at 300 °C exhibits a capacitance of 0.88 μF/cm^2 at 1.0 Hz, indicating a much higher capacitance than those of SiO_2 with the same thickness owing to the sufficient formation of the electrical double layer (EDL) with mobile protons in the dielectric layer. IGZO TFTs on silica dielectric layers annealed at 300 °C exhibited hysteresis characteristics. Counterclockwise hysteresis resulting from the slow relaxation of accumulated protons between the dielectric and channel interface was observed. Additionally, the remarkable repeatability of the electrical performance in ambient air was maintained. To test neuromorphic behavior, pair pulse facilitation (PPF) was emulated with a bottom gate as the presynaptic terminal and the IGZO channel as the postsynaptic terminal. With a time interval (Δt) of 40 ms, 1.99 PPF was observed

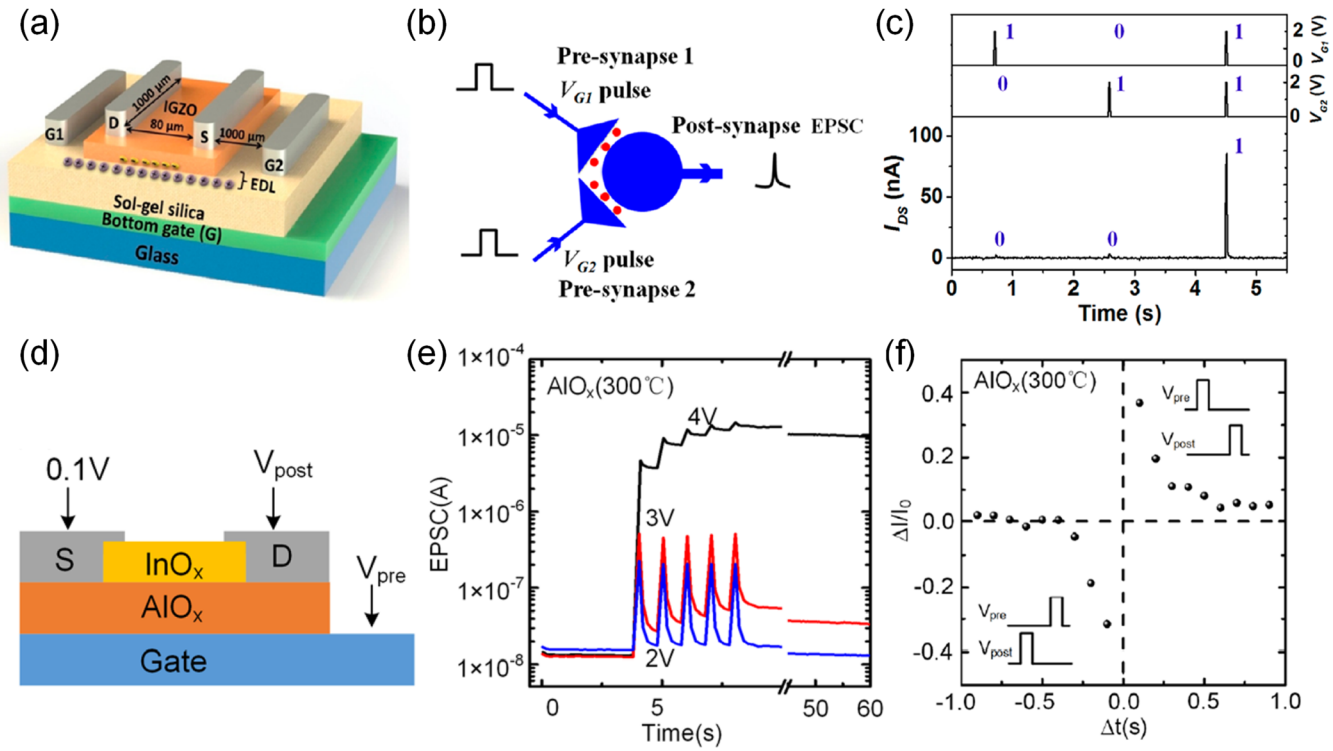

FIG. 12. (a) Schematic image of the IGZO-based EDL transistor gated by the sol-gel processed silica film with one bottom gate electrode and two in-plane gate electrodes. (b) Schematic image of the spatial summation of two presynaptic inputs in a biological neuron. (c) EPSCs triggered by the presynaptic spikes of 2.0 V and 20 ms applied on two in-plane gates of G1 and G2. EPSCs were measured at V_{DS} = 0.5 V. Reproduced with permission from Shao *et al.*, ACS Appl. Mater. Interfaces **8**, 3050 (2016). Copyright 2016 American Chemical Society. (d) Schematic diagram showing the structure of an AlO_x/InO_x synaptic transistor. (e) EPSCs stimulated by the pulses with various amplitudes (2–4 V) for the transistor gated by AlO_x (300 °C). (f) $\Delta I/I_0$ as a function of Δt, where $\Delta I = I_{STDP} - I_0$; Δt is the interval between the presynaptic spike and the postsynaptic spike. Reproduced with permission from Liang *et al.*, Appl. Phys. Lett. **116**, 012102 (2020). Copyright 2020 AIP Publishing.

because more ions can accumulate in the dielectric/channel interface after the second presynaptic pulse was applied. The spatial summation behavior of the synaptic device was also tested, as shown in Fig. 12(b). By implementing lateral gated electrodes (G1 and G2) simultaneously, a large EPSC of 86 nA was measured compared to the singular triggering of individual presynaptic pulses (3 nA), mimicking the superlinear summation property of synaptic behavior in biological systems [Fig. 12(c)].[97] This study proved that an electrical double layer derived from a sol-gel processed dielectric layer can be used to express neuromorphic characteristics in metal oxide TFTs.

Liang *et al.* demonstrated neuromorphic devices using the solution-processed AlO_x dielectric and InO_x semiconductors, as shown in Fig. 12(d).[94] A lower annealing temperature of solution-processed AlO_x can form a higher concentration of hydrogen ions, acting as a neurotransmitter that can be absorbed and desorbed according to the gate pulse.[98] Because of the higher concentration of hydrogen ions, hysteresis in the counterclockwise direction

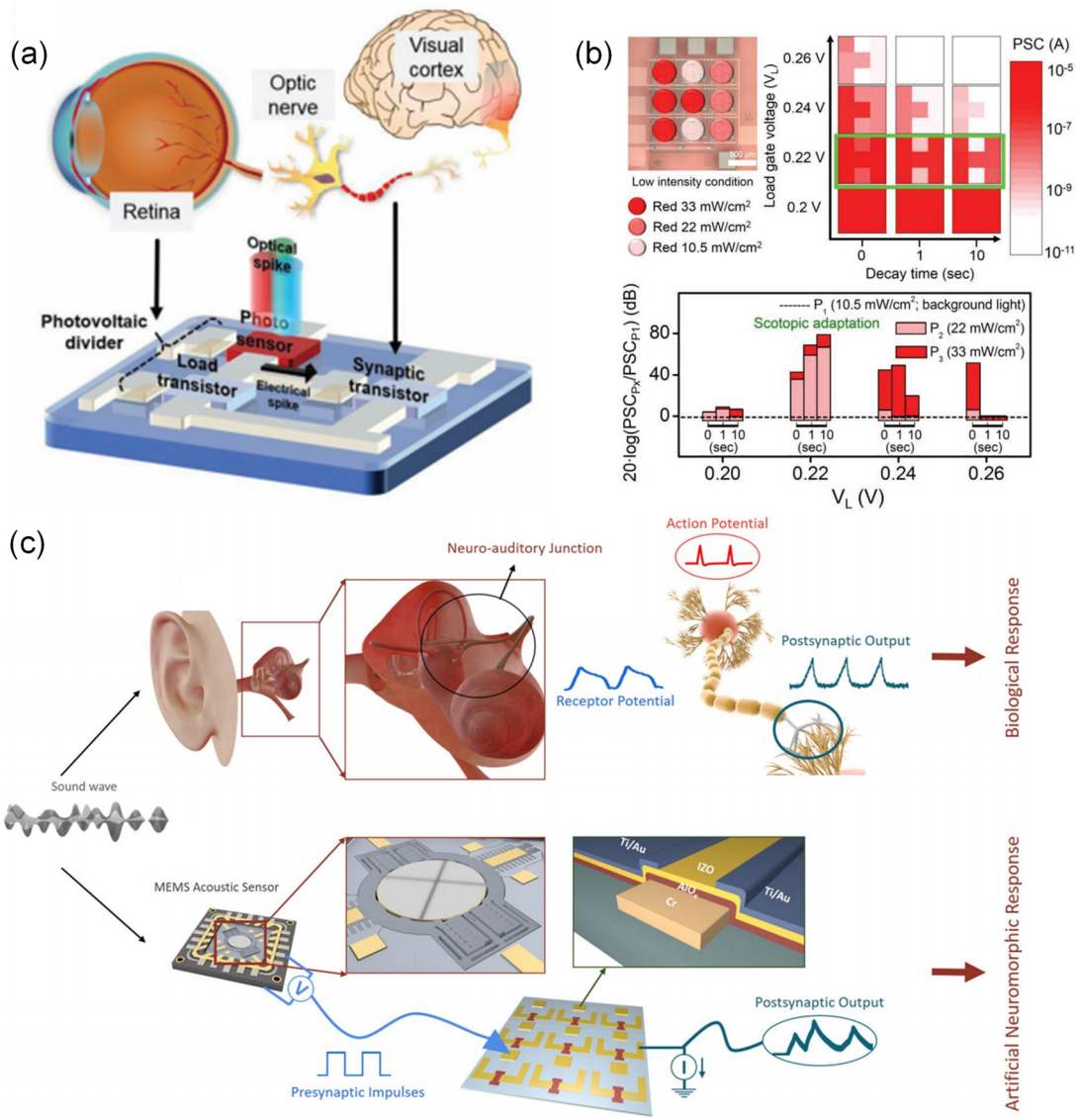

FIG. 13. (a) A light-adjustable optoelectronic neuromorphic circuit for the emulation of artificial visual perception system. (b) The 3 × 3 optoelectronic neuromorphic circuit array image, encoded images in the array are immediately recoded after light irradiation, and time-dependent PSC decibel levels under low-intensity (10.5–33 mW/cm^2) red illuminance gradation, respectively. For the PSC decibel levels, P_1–P_3 represent red-light intensities of 10.5, 22, and 33 mW/cm^2, respectively. Reproduced with permission from Kwon *et al.*, Adv. Mater. **31**, 1906433 (2019). Copyright 2019 John Wiley and Sons, Inc. (c) Schematic demonstration of acoustic signal processing, schematic representation of the action potential creation in the human body as a result of the incoming acoustic stimulation, and acoustic signal processing system employing synaptic transistors with printed AlO_x dielectrics. Reproduced with permission from Bolat *et al.*, Sci. Rep. **10**, 16664 (2020). Copyright 2020 Springer Nature.

was observed in the TFT performance with AlO_x annealed at 300 °C. Various gate pulses were applied to confirm the neuromorphic behavior. As the interval between the first and second pulses increases, the second EPSC approaches the same value as the first EPSC. When several stronger (4 V) synaptic gate pulses were applied, the highest EPSC with a long-term plasticity (LTP) of 1×10^{-5} was achieved. Spike timing-dependent plasticity is an important parameter for describing the synaptic plasticity of devices, mimicking the synaptic function,[99] relying on the order of presynaptic and postsynaptic arrival. As shown in Fig. 12(f), the value of $\Delta I/I_0$ increases when the duration Δt decreases because of the desorption of proton ions. From the low-temperature processed AlO_x, a high concentration of hydrogen ions in the dielectric layer activated neuromorphic devices by emulation of synaptic functions.

Inorganic solid electrolytes have great potential in terms of high capacitance and stability.[100] Ren *et al.* demonstrated photoperception neuromorphic transistors emulating human cognitive behavior via the solution-processed mesoporous silica (MSC) dielectric layer.[96] The fabricated dielectric films exhibit a high capacitance of 2.5 $\mu F/cm^2$ at 1 Hz with a reliable frequency dependency. Because of mobile protons in the MSC, a low operational voltage of TFTs below 1.5 V with a hysteresis loop was achieved. The potentiation and depression behaviors were observed through the pulsed gate input. A stronger amplitude of the signal input produces a larger postsynaptic current (PSC) output, suggesting that strong memory is held for a long time. Selective memory behavior has been mimicked using successive positive or negative presynaptic signals. Based on the developed neuromorphic system, they emulate the cognitive perception system of taste aversion learning for cigarettes in the judgment between craving and aversion. This study demonstrated that artificial perception learning systems can be enabled by solution-processed solid-state oxide dielectrics.

An environmentally adaptive artificial vision system can also be realized using a combination of light adaptive sensors and neuromorphic devices. Kwon *et al.* demonstrated optoelectronic neuromorphic circuits using a sodium aluminum oxide (SAO) dielectric layer.[93] The optical spike was converted into an electrical spike by using the CdSe light sensor, and the generated V_{Spike} was transferred to the synaptic transistor with SAO dielectrics [Fig. 13(a)]. In the SAO dielectric, Na^+ ions are used as neurotransmitters, and some Na^+ ions can be trapped in the channel layer via strong and repetitive gate pulses. The size of the PSCs according to the illumination pulse of the optoelectronic neuromorphic device was observed, indicating that different V_{Spike} values can be applied depending on the wavelength and intensity of the light. To demonstrate their reliable spike-timing-dependent plasticity (STP) and LTP performance, the photopic and scotopic adaption of neuromorphic devices was evaluated in a 3×3 array under bright and weak light conditions, as shown in Fig. 13(b). By controlling the load voltage (V_L) as a visual threshold, the successful differentiation of visual images in bright and weak light conditions was confirmed. This study proved that the combination of optoelectronic and neuromorphic devices can emulate highly susceptible human-like visual recognition, regardless of changes in environmental background light conditions.

Bolat *et al.* reported synaptic transistors with printed AlO_x dielectrics in the application of acoustic signal processing systems.[95] Figure 13(c) shows a schematic of sound processing (top) in the human body and the designed sound signal-processing system (bottom). The printed AlO_x dielectric with the IZO semiconductor exhibits the hysteresis behavior of the transistor, which is typical of the memory characteristics of TFTs.[101,102] In the solution-treated aluminum oxide dielectric, large amounts of hydrogen were shown to be the main cause of the adsorption/desorption of water and the water present in the bulk of the dielectric, as well as counterclockwise hysteresis.[70] The received sound wave is converted into a square wave of the same frequency, and the square wave acts as the input signal of the transistor. To demonstrate the synaptic behavior of the transistor, the EPSC performance of neuromorphic devices was tested at a 50 kHz input signal. Additionally, the potentiation and/or depression property was demonstrated using a sound wave input as a presynaptic pulse at 10 kHz sound. The charge trapping property in the printed AlO_x dielectric creates memory-like ferroelectricity in the transistor, enabling a synaptic operation of up to 50 kHz and covering the entire audio frequency range. The demonstration of high-speed acoustic synaptic responses reveals enormous potential applications for high-performance neuroacoustic signal processors.

III. RESISTIVE SWITCHING MEMORY

Owing to the rapid growth of portable devices and the popularity of IoT technology networks in recent years, the tremendous demand for communication and computation data storage continues to increase exponentially. Along with dynamic random access memory (DRAM) and flash memory, which occupy the largest scale in the memory technology market, resistive random access memory (ReRAM) has attracted considerable attention as a competitive nonvolatile memory (NVM) technology. It combines the advantages of a simple device structure, fast switching rate, high endurance, and good retention time.[103,104] ReRAM has been studied based on the structural platform of cross-bar architecture to realize higher density storage than other types of RAM [e.g., ferroelectric RAM (FeRAM), phase-change RAM, and magnetic RAM (MRAM)]. ReRAM uses the reversible resistive switching (RS) effects of the material, and when a specific electrical sweep bias (or E-field) is applied, the changes in electrical resistivity between different stable states [a high-resistance state (HRS) and a low-resistance state (LRS)] are stored as data. The fabrication of metal oxide-based ReRAM devices has been extensively reported for use with various memory structures fabricated via several deposition techniques, including atomic layer deposition (ALD),[105,106] chemical vapor deposition (CVD),[107,108] physical vapor deposition (PVD),[109,110] and chemical solution deposition (sol-gel) methods.[10] Compared to conventional vacuum-based deposition methods, ReRAM devices using sol-gel methods have significant advantages in cost-effective manufacturing, simple step fabrication, and large-scale and mass production.[10]

Their reversible changes in resistance and switching mechanisms have been demonstrated based on various materials, such as transition metal oxides, complex perovskite oxides, conductive cationic amorphous materials, and organic/polymers.[10,111–114] Among them, transition metal oxides have been actively developed and researched, and it is possible to achieve excellent performances, such as low power consumption, high on/off ratio (over

3–4 orders of magnitude), good device reliability, and ease of integration with existing CMOS technology.[11] Their switching behaviors have been demonstrated in various dielectric oxide materials, especially in the binary oxide system—NiO,[115–120] TiO_2,[121–125] HfO_2,[126–132] ZrO_2,[133–137] Al_2O_3,[138–145] CoO,[146–148] Ta_2O_5,[149,150] and SiO_2[151,152]—because of their simple and controllable composition and stoichiometry. Moreover, ternary oxide systems (e.g., $SrTiO_3$,[153–155] $CaTiO_3$,[156] $PbZrO_3$,[157] $BaTiO_3$,[158,159] spinel ferrite-related oxides,[160–163] and multiferroic $BiFeO_3$[164,165]) and other complex oxide systems[166] have been studied. Table III shows the different processing conditions and properties of sol-gel metal oxide thin films according to the types of substances used in ReRAM devices in the literature. Extensive research on sol-gel ReRAM devices has been conducted in recent years on the preparation and fabrication of transition metal oxides with careful consideration of their chemical and electrical properties. This Research Update reviews recently reported sol-gel oxide thin films for ReRAM devices with various metal components. In particular, we discuss the recent progress in the development of low-temperature sol-gel metal oxide ReRAM devices on flexible plastic substrates and the challenges involved over the past five years (cf. additional key review and the work of Carlos *et al.*[10] for detailed information for solution-based oxide resistive switching memory devices).

A. Design of materials and structures

As previously discussed, sol-gel-based metal oxide ReRAM devices have been extensively researched and developed owing to the unclear physical mechanism, which is still debated, and several device reliability issues during the repeated operation, such as nonuniformity of RS parameters, high electroforming voltage, large and unstable fluctuation in HRS and LRS, and degeneration of endurance properties and retention time. Many research approaches, such as metal doping,[10,148,167–170] introducing metal[148,171,172] or metal oxide[115,116,120,127,129] nanoparticles (NPs), bi- and multilayer structures,[119,135,173] and different atmospheric conditions,[126,133,137,146,171] have been long been reported as solutions. We present several studies dealing with the recently reported sol-gel-based metal oxide materials, including RS effects with additional functions, and the relationship between basic approaches of sol-gel chemical reactions and their RS changes in ReRAM devices.

1. Multifunctional oxides for resistive and magnetization switching

Yao *et al.* reported the synthesis of various metal oxide systems, including simple binary oxides to complex oxides by using a sol-gel process with different annealing conditions for improving RS effects and performance, such as a lower forming voltage and uniform distribution of switching voltages, excellent endurance, and data retention time. They reported that sol-gel solution-derived spinel Co_3O_4 thin films[146] with different annealing atmospheres (such as oxygen, air, and nitrogen) and temperatures[147] show effects on the properties of RS and magnetic modulation. They also demonstrated that the switching mechanisms of RS behaviors can be explained by the formation and rupture of oxygen vacancies based on conducting filaments (CFs) via the temperature-dependent resistance and magnetization variations of Co_3O_4 thin films. Furthermore, they embedded Ag-metal nanoparticles into pure Co_3O_4 thin-film devices[148] to promote the local electric field, oxygen vacancies, and conversion of cation valence states (Co^{2+} and Co^{3+}). The different approaches of the synthesized Co_3O_4 thin films demonstrated both resistive and magnetization switching properties, which represent a feasible approach for designing multifunctional electromagnetic coupling NVM devices. They further studied sol-gel solution-based different magnetic spinel-ferrite complex ternary metal oxide materials, especially $NiFe_2O_4$, for use in promising applications of multifunctional electric- and magnetic-integrated devices with the switching mechanism of RS behaviors from the formation and rupture of CFs along the preferential orientation growth direction.[174] Subsequently, they introduced various rare-earth ions (Ce,[160] Gd,[161] and Cr[162]) into spinel ferrite devices to improve the RS properties. Finally, they proposed the underlying switching mechanism by which the resistive and associated magnetization switching effects of rare-earth ion doping can be ascribed to a suitable concentration of oxygen vacancies and conversion of cations (e.g., ion valence change, redox reaction, and Joule heating effects)[161,174–178] while minimizing randomness for the formation/rupture of CFs.[160–163]

2. Sol-gel oxide solution aging and interfacial oxide layer for ReRAM devices

Hsu *et al.* comprehensively investigated the effects on the aging time of sol-gel precursor solution of HfO_x—ranging from 1 to 150 days—and the RS behaviors of the HfO_x ReRAM devices.[128] The as-prepared and semitransparent sol-gel solution of HfO_x turned to a completely dissolved and transparent solution after aging for 60 days, presenting the optimal ReRAM device performance. On the other hand, the HfO_x ReRAM devices using the sol-gel solution that aged for 150 days (over 90 days) showed high-instability RS behaviors due to more defect states in the device and required a high transition voltage to inject more carriers to fill the traps. Next, they explored the effects of bottom electrodes (BEs) on the RS behavior of sol-gel HfO_x thin films to reduce the sol-gel aging time (from 60 to 3 days) and to improve the ReRAM device performance.[126] They considered the Gibbs free energy of the interfacial oxide layer between the deposited HfO_x (ΔG of HfO_2 formation ~ −1010.8 kJ/mol)[179] and three metal BE layers (Al, Mo, and Pt). Al created abundant oxygen vacancies by capturing the oxygen in the HfO_x film because of the low Gibbs free energy of the AlO_x interlayer (ΔG of Al_2O_3 formation ~ −1582 kJ/mol),[180] making the HfO_x film conductive. However, Pt resulted in the HfO_x film being nonconductive because of the high Gibbs free energy of the PtO_2 interlayer with nonspontaneous reactions with oxygen. Interestingly, the moderate value of the Gibbs free energy of the MoO_x interlayer (ΔG of Mo as the BE ~ −443.8 kJ/mol)[181] from Mo BE could induce sufficient oxygen vacancies in the HfO_x film, leading to stable RS characteristics with a maximum process temperature of 100 °C.[126]

B. Approaches for low-temperature fabrication

Most studies of sol-gel-based metal oxide films for memory applications have been reported in a template based on the

TABLE III. Parameters of resistive memory devices using the sol-gel metal oxide dielectric layer. [T_P: maximum processing temperature, t_P: processing time, TE/BE: top and bottom electrode, U/B: resistive switching behaviors of unipolar and bipolar, NP: nanoparticle, STO: strontium titanate, STN: strontium titanate nickelate, DI: dip coating, AN: anodization (anodic oxidation), IM: imprinting method, PET: polyethylene terephthalate, PI: polyimide, and O_2, N_2, Air: annealing in oxygen, nitrogen, and air condition.]

Year	Material	Deposition	T_P (°C)	t_p (min)	TE/BE	U/B	$R_{ON/OFF}$	Retention time (s)	Endurance (cycle)	Processing feature (substrate, if flexible)	Bending time (if flexible)
					Group TiO and STO						
2017[121]	TiO_2	SC	400	60	Pt/Pt	B	5.5×10	···	500		
2017[184]	TiO_2	DI	150	180	ITO/Pt	B	10^3	10^4	600		
2018[122]	TiO_2	AN	RT	ND	Ti/Ag	B	2.7×10	···	16	DUV (PET)	1000
2018[123]	TiO_2	AN	RT	ND	Ti/Cu	B	8×10	-	···		
2019[124]	TiO_{2-x}	AN	RT	ND	Ti/Pt	B	$\sim 10^2$	-	4500		
2021[125]	TiO_2	SC	RT	300	ITO/Ag	B	>10	2×10^3	100	DUV (PET)	40
2017[153]	Fe:STO	SC	700	60	ITO/Au	U	$\sim 10^5$	10^4	50		
2017[154]	STN	SC	100	15	ITO/Al	B	10^5	10^5	140	(PET)	14
2018[155]	STO	SC	650	60	ITO/Au	U	10^3	10^4	···		
					Group CoO and FeO						
2019[146]	Co_3O_4	SC	600	60	Pt/Pt	B	$\sim 10^2$	10^4	800	O_2, N_2, air	
2019[147]	Co_3O_4	SC	600	60	Pt/Pt	B	$\sim 10^2$	10^4	300		
2019[148]	Ag:Co_3O_4	SC	600	60	Pt/Pt	B	$\sim 10^2$	2×10^4	1500		
2017[160]	Ce:$NiFeO_4$	SC	750	60	Pt/Pt	U	10^3	10^5	500		
2017[161]	Ga:$NiFeO_4$	SC	750	60	Pt/Pt	U	10^2	10^5	500		
2019[162]	Cr:$NiFeO_4$	SC	700	60	Pt/Pt	B	10^2	10^5	500		
2020[163]	$Yt_3Fe_5O_{12}$	SC	700	60	Pt/Pt	U	10^2	10^4	200		
					Group ZrO and HfO						
2017[133]	ZrO_2	SC	500	60	ITO/Ti	B	7×10	10^4	100	O_2	
2017[134]	ZrO_2	DI	150	180	ITO/Pt	B	10^5	10^4	600	DUV (PET)	1000
2018[135]	ZnO/ZrO_2	SC	300	60	Al/Al	B	$\sim 10^3$	···	20		
2018[136]	ZrO_x	SC	400	60	n + Si/In	B	$\sim 10^3$	10^4	500		
2020[137]	ZrO_2	SC	200	60	Al/Al	B	$\sim 10^4$	10^4	150	O_2 (PI)	150
2017[126]	HfO_x	SC	350	60	Mo/In	B	~10	···	200	O_2	
2017[128]	HfO_x	SC	100	10	Mo/In	B	2.71	···	500		
2017[127]	HfO_2 NP	IJ	240	180	Au/Ag	B	10^3	···	128	Vacuum	
2018[129]	HfO_2 NP	BL	ND	ND	Pt/Pt–Ir	B	10^5	···	50		
2018[130]	HfO_2	AN	RT	ND	Hf, Nb/Pt	B	5	10^4	1000		
2019[131]	Nb:HfO_x	AN	RT	ND	Hf–Nb/Pt	B	5	10^4	1000		
2021[132]	HfO_x	AN	RT	ND	Hf/Pt	B	···	10^6	10^4		
					Group NiO and AlO						
2017[115]	NiO/ZnO NP	SC	150	120	ITO/GaIn	B	10^3	···	1000	(PET)	1000
2018[116]	NiO NP	IM	80	10	Pt/Pt	U	10^5	···	···	(PET)	···
2018[117]	NiO	SC	200	30	Pt/Ag	B	10^5	10^4	80	DUV	
2018[118]	NiO	SC	350	30	Pt/Ag	B	>10	10^4	100	SCS	
2018[119]	NiO/CeO_2	SC	400	120	ITO/GaIn	B	$\sim 10^3$	···	100		
2020[120]	NiO NP	SC	180	60	Ni/Ni	U	$\sim 10^3$	···	120	(PI)	120

TABLE III. (*Continued.*)

Year	Material	Deposition	T_P (°C)	t_p (min)	TE/BE	U/B	$R_{ON/OFF}$	Retention time (s)	Endurance (cycle)	Processing feature (substrate, if flexible)	Bending time (if flexible)
					Group NiO and AlO						
2018[138]	AlO_x	SC	565	2	Pt/Ti	B	4×10^2	10^4	100	Microwave	
2018[139]	AlO_x	SC	347	2	Pt/Ti	B	10	10^4	1000	Microwave	
2018[140]	Al_2O_3	SC	500	30	Pt/Ti	U	$\sim10^5$	10^5	100	SCS	
2019[141]	AlO_x	SC	170	30	Foil/Al	B	$\sim10^3$	10^4	100	(Foil)	500
2019[142]	AlO_x	SC	RT	30	ITO/Ag	U	$\sim10^3$	10^4	100	DUV (PET)	200
2019[143]	AlO_x	SC	200	60	Pt/TiN	B	1.8×10^2	10^4	30		
2020[144]	AlO_x	SC	250	60	ITO/Ag	B	$\sim10^3$	10^4	500		
2021[145]	AlO_x	IJ	150	90	ITO/Ag	B	4×10	10^5	100	DUV + SCS	
					Group TaO and group SiO						
2017[149]	TaO_x	AN	RT	⋯	Ta/Pt	B	>10	10^4	10^6		
2020[150]	TaO_x	AN	RT	⋯	Ta/Pt	B	8×10	⋯	⋯		
2019[151]	Bi_2SiO_5	SC	600	60	Pt/Pt	B	10^2	10^4	100		
2020[152]	SiO_x	SC	RT	30	Au/Ag	B	10^8	$>10^4$	349	DUV (PI)	2000

well-known RS operation principle and the performance of classical metal oxide materials.[10,112,182,183] The conventional fabrication of metal oxide films exhibiting RS properties requires long-duration processing time (>1 h) and temperature over 400–600 °C. To overcome, many studies have been focused on the low-temperature formation of high quality oxide film processing methods and advanced approaches from convergent perspectives of material chemistry.[10,33]

1. Solution combustion synthesis with DUV treatment for ReRAM devices

As previously discussed in Sec. II, the formation and densification of the sol-gel metal oxide layer require high thermal annealing temperatures to build sufficient structures of the metal oxide frameworks for the removal of organic impurities and unreacted chemical species, leading to high-quality films. Carlos *et al.* developed a unipolar resistive switching aluminum oxide (Al_2O_3) device using a simple solution combustion synthesis (SCS) process for the first time.[140] The SCS methods can promote the conversion reactions from metal precursors into metal oxides accompanied by exothermic redox reactions during the annealing process to reduce the required external thermal budget. They prepared high-quality amorphous Al_2O_3 thin films (bilayer structure) at 500 °C on a transparent conducting oxide (TCO) glass substrate for fully transparent ReRAM devices, which have good endurance and reliable retention time (~10^4 s), and multilevel cell (MLC) operation. The same research group next simultaneously combined different methodologies such as thermal annealing with SCS at 150 °C and DUV treatment to improve the electrical performance and compatibility with the printing industry.[145] The inkjet-printed SCS-based aluminum oxide RS devices, by combining the DUV treatments, presented a bipolar RS behavior with good endurance and retention time (10^5 s), high reproducibility, and a sufficient on/off ratio to achieve a MLC with at least four distinct level states [Figs. 14(a)–14(c)]. The overall results presented the outlooks for large-area manufacturing of sol-gel ReRAM devices with a high resolution-printing method and low-temperature processing techniques, which are suitable for low-cost substrates (e.g., plastic or paper).

2. Microwave irradiation for ReRAM devices

Cho and co-workers[138,139] employed the microwave irradiation method for the fabrication of sol-gel solution-based AlO_x-based ReRAM devices. As a low-temperature sol-gel method, microwave irradiation has attracted attention for achieving good energy transfer efficiency for the target metal oxide materials to induce molecular motions and rearrangements at the atomic scale. The microwave irradiation method has different advantages, such as short processing time, good thermal uniformity, selective heating, and efficient removal of metal oxide defects. They controlled the microwave power ranging from 600 to 3000 W for the post-deposition annealing process to optimize the formation of the AlO_x active layer. As the microwave power increased, the microwave-assisted AlO_x ReRAM devices exhibited a significant improvement in the memory window and good reliability (endurance over 10^3 cycles and a retention time of 10^4 s at RT) with multilevel operation.

3. Electrochemical anodization method for ReRAM devices

Recently, anodization has attracted attention because it is a low-temperature and cost-efficient process that can be used to fabricate high-quality and dense oxide thin films (e.g., pinhole-free) on

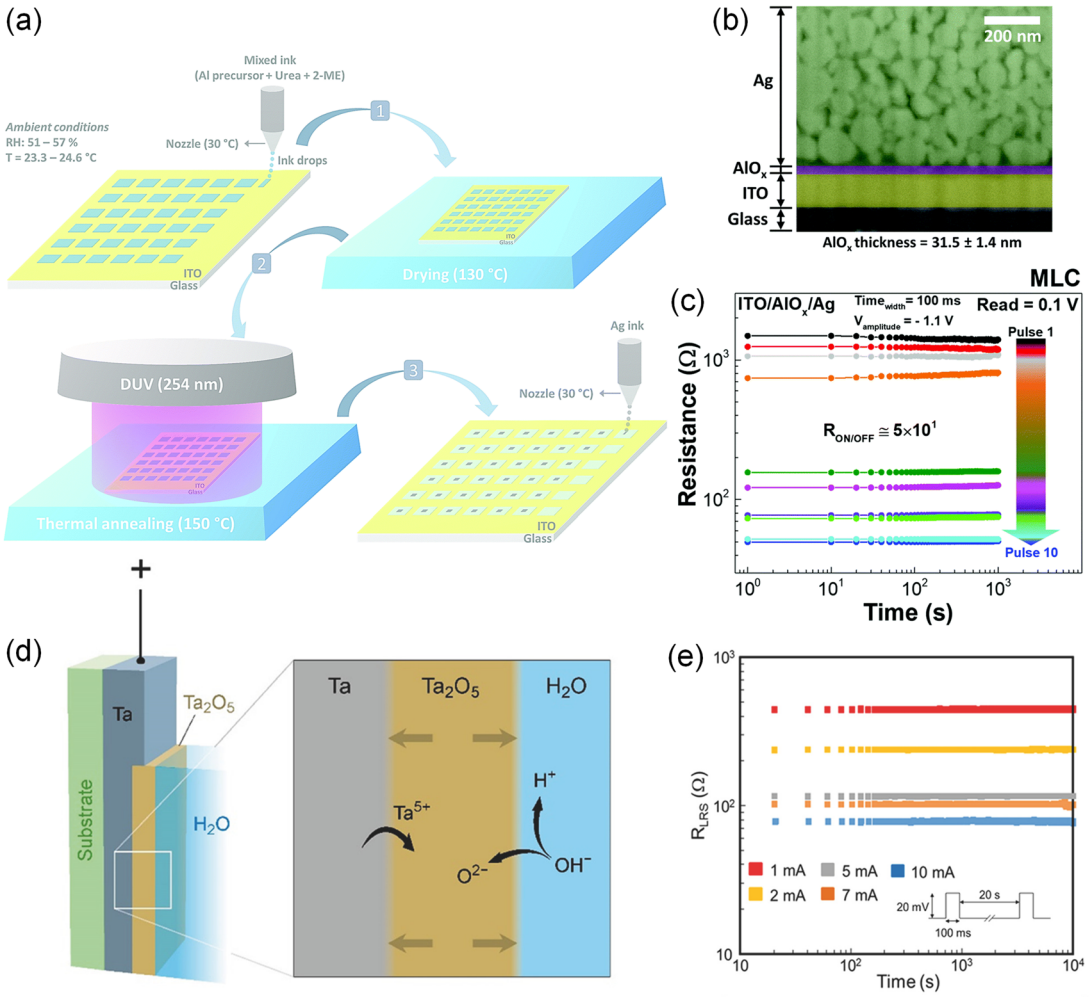

FIG. 14. (a) Schematic of the printing steps of the SCS solution-based metal oxide resistive switching memory device: (i) inkjet-printing process of the AlO_x ink atop of ITO glass, (ii) drying process after printing, (iii) DUV photo-assisted annealing process of the SCS-AlO_x thin film, and (iv) inkjet printing of the Ag nanoparticle ink. (b) High-resolution SEM-FIB cross-sectional image of the fabricated resistive switching memory device. (c) The multistage storage [multilevel cell (MLC)] properties on the reset side by the application of a current visible pulse (10 pulses) stress (CV-PVS) with a time width of 100 ms. Reproduced with permission from Carlos *et al.*, J. Mater. Chem. C **9**, 3911 (2021). Copyright 2021 Royal Society of Chemistry. (d) Schematic of the preparation of the electrochemical growth of the anodic Ta_2O_5 layer on the Ta metal electrode layer. (e) Retention test of the LRS for five current compliances applied during the SET cycle in the test (20 mV pulse at every 20 s with 100 ms READ pulse). Reproduced with permission from Zaffora *et al.*, Adv. Mater. **29**, 1703357 (2017). Copyright 2017 John Wiley and Sons, Inc.

various metallic substrates with (1) precise control over morphology and thickness and (2) tailored structural and electronic properties.[150] The redox-based ReRAMs constitute the metal/solid electrolyte/metal junctions. Zaffora *et al.* reported redox-based ReRAM devices electrochemically prepared by anodizing sputtering-metal films in buffer solution for the formation of metal oxides of Ta/Ta_2O_5,[149] Hf/HfO_2, and Nb/Nb_2O_5[130] and mixed oxides of Ta–Al and Hf–Nb.[131] The electrochemically anodized Ta/Ta_2O_5-based memory devices[149] demonstrated excellent performance [i.e., high endurance $>10^6$ cycles, data retention $>10^4$ s, and fast switching rate (~ns)] [Figs. 14(d) and 14(e)]. Furthermore, unlike the Nb/anodic Nb_2O_5/Pt device cells, the fabricated Hf/anodic HfO_2/Pt device cells showed excellent device reliability and performance (endurance $> 10^3$ cycles, retention time $>10^4$ s, and MLC with >5 different values),[130] demonstrating that electrochemical growth of the anodic oxides in various conditions demonstrated potential to produce high quality and reliable oxide thin films for ReRAM device applications.

C. Flexible memory devices

The maximum processing temperature for the fabrication of flexible and stable ReRAM devices directly depends on the endurance temperature and internal thermal stress resistance

of many polymer substrates. However, most sol-gel solution-based metal oxides require a high thermal budget (>400 °C), which is not fully suitable for the poor heat resistance of polymer substrates, such as PI, PES, PEN, and polyethylene terephthalate (PET). The above-mentioned studies on the development of low-temperature sol-gel-based oxide film materials and fabrication techniques for ReRAM devices eventually exhibit superior and reliable performance even on flexible plastic substrates despite intense mechanical stress (e.g., bending radius and times).

1. UV photochemical activation

Conventional sol-gel methods for the preparation of high-performance ReRAM devices require a high-temperature annealing process, which will hamper processing compatibility with flexible substrates owing to their poor thermal endurance. For instance, commercially available and low-cost flexible substrates such as PET should be handled at temperatures below 150 °C. Since the report of the DUV photochemical solution method[56,57] for low-temperature oxide film fabrication, many studies on the fabrication of various

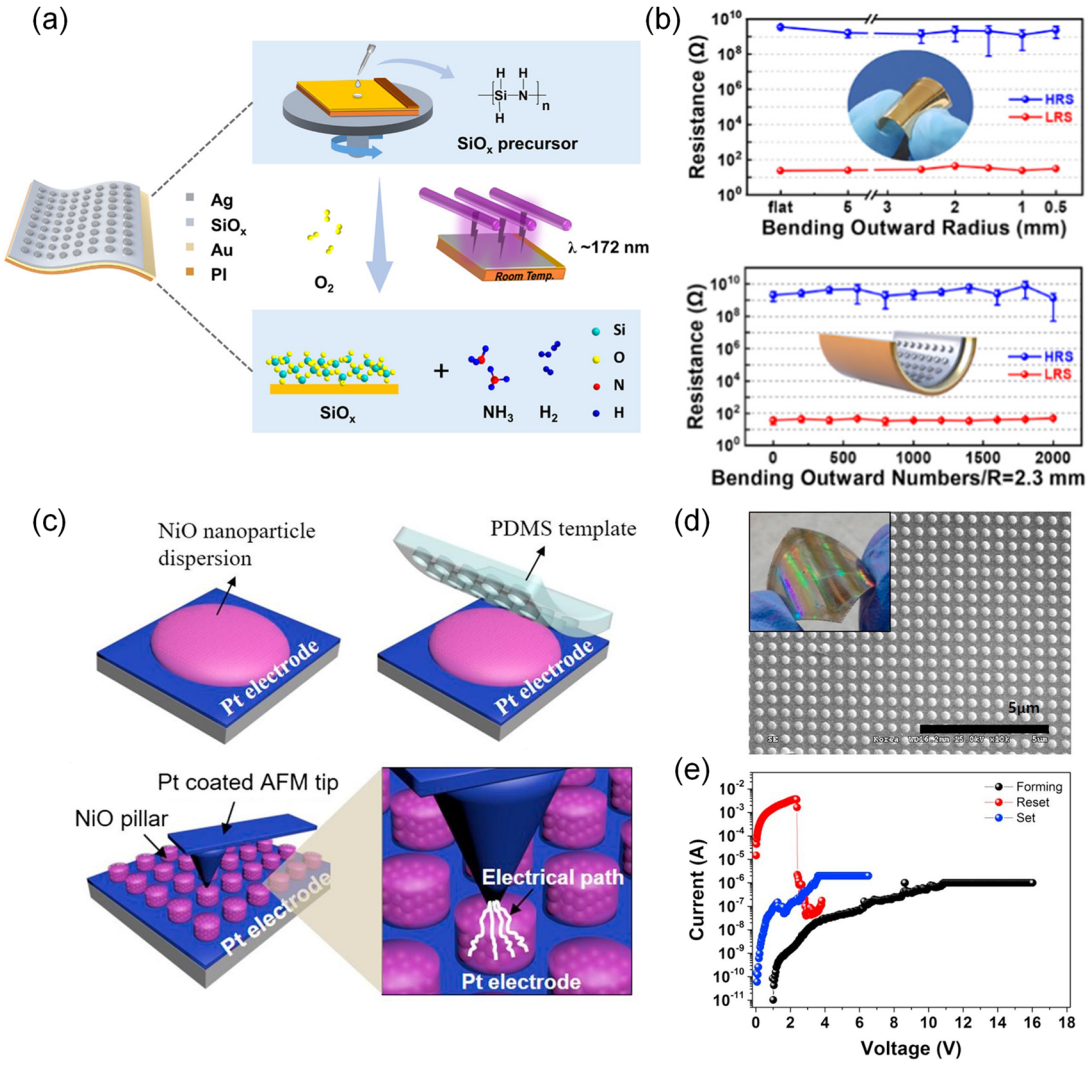

FIG. 15. (a) Schematic of the preparation of the flexible Ag/SiO_x/Au/PI device and the conversion of PHPS into SiO_x under vacuum ultraviolet irradiation ($\lambda \sim 172$ nm). (b) The resistance of HRS and LRS with varying the bending outward radius in the range of flat to 0.5 mm and the change in resistance with bending numbers in the inward direction, $R = 2.3$ mm, with compressive bending states of the samples. Reproduced with permission from Li *et al.*, ACS Appl. Mater. Interfaces **12**, 56186 (2020). Copyright 2020 American Chemical Society. (c) Schematic illustration of the fabrication process of NiO NP-based resistive memory devices by the direct imprinting method. (d) SEM image of the flexible NiO NP-based resistive memory devices on a flexible PET substrate. (e) *I–V* curves of the resistive switching behaviors of NiO NP-based flexible memory devices. Reproduced with permission from Kim *et al.*, Solid-State Electron. **142**, 56 (2018). Copyright 2018 Elsevier.

metal oxide films with resistive switching behaviors on flexible plastic substrates (such as PET) have been reported. Li *et al.*[134] demonstrated a sol-gel ZrO_2 layer on a PET/ITO substrate via a low-temperature DUV photochemical process and a UV-assisted micropatterning technique for the fabrication of flexible ReRAM miniature device arrays. They employed two types of UV illumination with 325–365 nm and 185 and 254 nm for micropatterning of photosensitive sol-gel films and for further condensation reactions. The ZrO_2 layers on the flexible PET/ITO substrate showed excellent memristive properties with a high ratio of the on/off state and stable performance with 10^3 bending times and 6.25 mm bending radius. Using the low-temperature UV photochemical solution method, Duan[142] and Zou[125] also reported the fabrication of AlO–OH and TiO_2 thin films for flexible resistive memory on PET/ITO substrates with good unipolar RS behaviors and long retention times and mechanical endurance with different bending radii and times. Their results showed that DUV-photochemical activated flexible ReRAM devices have potential applications in neural networks and wearable electronics.

Li *et al.*[152] demonstrated the fabrication of an amorphous and uniform SiO_x layer by the efficient conversion of an inorganic polymer from perhydropolysilazane (PHPS) into SiO_x via vacuum ultraviolet (VUV) irradiation ($\lambda \sim 172$ nm) at room temperature on a PI film for flexible ReRAM devices [Fig. 15(a)]. Interestingly, VUV irradiation of PHPS involved a photocleavage reaction of Si–N bonds and the subsequent oxidation reaction of the Si radicals, without undergoing typical sol-gel reactions of hydrolysis and condensation. The corresponding ReRAM devices of Ag/SiO_x/Au structures showed typical bipolar switching behavior with forming-free performance (349 cycles and resistance states $>10^4$ s at both RT and 85 °C). The device on a PI substrate showed outstanding flexibility with a minimum bending radius of 0.5 mm for 80 cycles, and no degradation of device performance was obtained after bending times (>2000 times) with a radius of 2.3 mm, which is the best among the reports on solution-processed binary oxide-based ReRAMs, even rival in the performance of vapor-deposited SiO_x devices [Fig. 15(b)]. They expected that highly flexible and stable ReRAM devices by the solution-based fabrication via VUV irradiation at room temperature have high potential in the application of smart wearable electronics.

2. Oxide NP solution deposition and ligand exchange process

Hong and co-workers demonstrated the simple fabrication of solution-based flexible ReRAM devices using NiO NPs[116,120] because the synthesized metal oxide nanoparticles do not require additional heat treatment for further crystallization. Moreover, they implemented the imprinting process using a demolded elastomeric PDMS template from the nanopatterned Si master stamp [Fig. 15(c)] for patterning of the NP solution.[116] Considering the capillary force and dewetting conditions, the NiO NP (20 wt. % NiO NPs in isopropyl alcohol solvent) was imprinted directly onto a flexible PET substrate with optimized pressure (5 bars) and temperature (80 °C) for 10 min. The fabricated flexible NiO NP ReRAM devices show good switching performances with a high on/off ratio resistance (~10^5) at 2.4 and 3.4 V for reset/set switching operation [Figs. 15(d) and 15(e)]. In a couple of years, they proposed improved NiO NP-based flexible ReRAM devices using the ligand exchange process from the original organic ligand to nitrosonium tetrafluoroborate ($NOBF_4$) ligand with relatively weak binding to NiO NPs, which allows their easy removal to promote agglomeration at a low temperature of 180 °C.[120] The NiO NP-coated substrate was immersed into the $NOBF_4$ solution (1 wt. % in dimethyl sulfoxide solvent) for 3 min and subsequent thermal treatment. The fabricated flexible NiO NP-based ReRAM devices on a flexible PI substrate exhibited excellent switching behaviors and stable resistance operation for more than 100 switching cycles under compressive stress with a bending radius of 10 mm, indicating the potential for next-generation flexible oxide memory devices.

IV. FERROELECTRIC MEMORY

In contrast to the metal oxide-based resistive switching memory devices that use the phenomenon of electrical resistance changes described in the previous chapter, the ferroelectric thin film devices in this Research Update are an electronic device that utilizes the following phenomenon: the polarization inside the thin film is not completely recovered and remains according to a given electrical field. Typically, ferroelectric oxide thin films are well known as multifunctional materials: (1) highly sensitive sensors and actuators on a small scale owing to their large electromechanical response and considering their large displacement capabilities and (2) nonvolatile memory applications [e.g., FeRAM and ferroelectric FET (FeFET)] owing to their high dielectric constants and large remnant polarization (P_r).[12,185]

As previously discussed, the processing advantages (such as cost efficiency and ease of controlling the film thickness, composition, and stoichiometry) that can be obtained through the fabrication of ferroelectric oxide thin films via the sol-gel method are identical to those of different applications of oxide thin films. However, a prerequisite for the fabrication of ferroelectric oxide thin films is that the ferroelectric components must undergo a crystallization process (including nucleation and growth) from the as-deposited film state.[12,13] Micro-/nanoscale structural properties (e.g., grain size and growth orientation; textures, secondary phase nucleation, and growth; and atomic vacancies and porosities) in the specified crystalline structures closely regulate the electrical performance of the synthesized ferroelectric metal oxide thin films.[12,13,186]

The development of classical ferroelectric oxide materials,[187] such as lead zirconate titanate [PZT or Pb(Zr and/or Ti and/or Ba)O_3] and strontium bismuthate tantalate (SBT), has been hindered because of the complex perovskite chemistry and high volatility of the main cations (Pb and Bi) during the crystallization process and downscaling and integration limitations with regard to compatibility issues in the fabrication of CMOS circuits.[12,185,188,189] Moreover, in these cases, they must be manufactured with a high film thickness because of a relatively low bandgap of ~3 eV and a feeble dielectric breakdown field in the thin film.[187] It also contains heavy metal elements (e.g., Pb), which can cause safety and environmental issues. Despite these shortcomings, they are still used in many electronic memory devices. In this Research Update, we review new chemical compositions or phase structures of various materials with unique properties (cf. additional key reviews[13,190] for

solution-based ferroelectric $BiFeO_3$ films and the first review report of solution-based ferroelectric HfO_2 films).

A. Sol-gel bismuth ferrite films

As a paradigmatic material candidate with lead-free (Pb-free) and strong ferroelectric properties, sol-gel-based bismuth ferrite ($BiFeO_3$ and BFO) has been extensively researched for the facile and low-cost preparation of high-quality large-scale thin films for next-generation ferroelectric NVM devices. However, the BFO thin films prepared by the sol-gel method have significant difficulties with robust ferroelectric properties, including a high leakage current from the structural defects, undesired formation of secondary phases (such as $Bi_2Fe_4O_9$), and crystallographic defects.[191] The fabrication of solution-based BFO thin films still has many challenges, such as (1) unsaturated and leaky polarization performances at room temperature and (2) randomly oriented crystallization within the whole bulk thin films.[190] To resolve these issues, the research progress of sol-gel solution-based BFO thin films has entered a new phase by employing strain engineering from specific metallic oxide electrodes and substrates (e.g., $SrTiO_3$, $DyScO_3$, $SrRuO_3$, $LaNiO_3$, $La_{0.7}Sr_{0.3}MnO_3$, or platinized silicon wafers) for high-quality epitaxial thin films in novel memory applications.[190,192–195]

From a different viewpoint of the conventional sol-gel method, Tomczyk *et al.*[196] reported the direct fabrication of the BFO thin films on polyimide flexible substrates using the seeded photosensitive precursor strategy, demonstrating the macroscopic performances of multiferroelectric switching at room temperature [i.e., $P_r \sim 2.8\ \mu C/cm^2$ and coercive field (E_c) ~ 0.38 MV/cm]. The proposed intermixed strategy with two low-temperature crystallization processes: (1) the preparation of crystalline nano-seeded diphasic sol/solution-gel precursors to promote the number of nucleation sites and (2) the synthesis of photosensitive precursors with UV-absorbing species (such as β-diketonates), followed by UV irradiation. This novel approach was successfully used to significantly reduce the crystallization temperatures of BFO films to as low as 300 °C and showed great potential for universal applicability to different complex metal oxides on flexible substrates in microelectronic devices [Figs. 16(a)–16(c)].

Furthermore, Bretos *et al.*[197] demonstrated the complementary strategies combining three chemical features for the

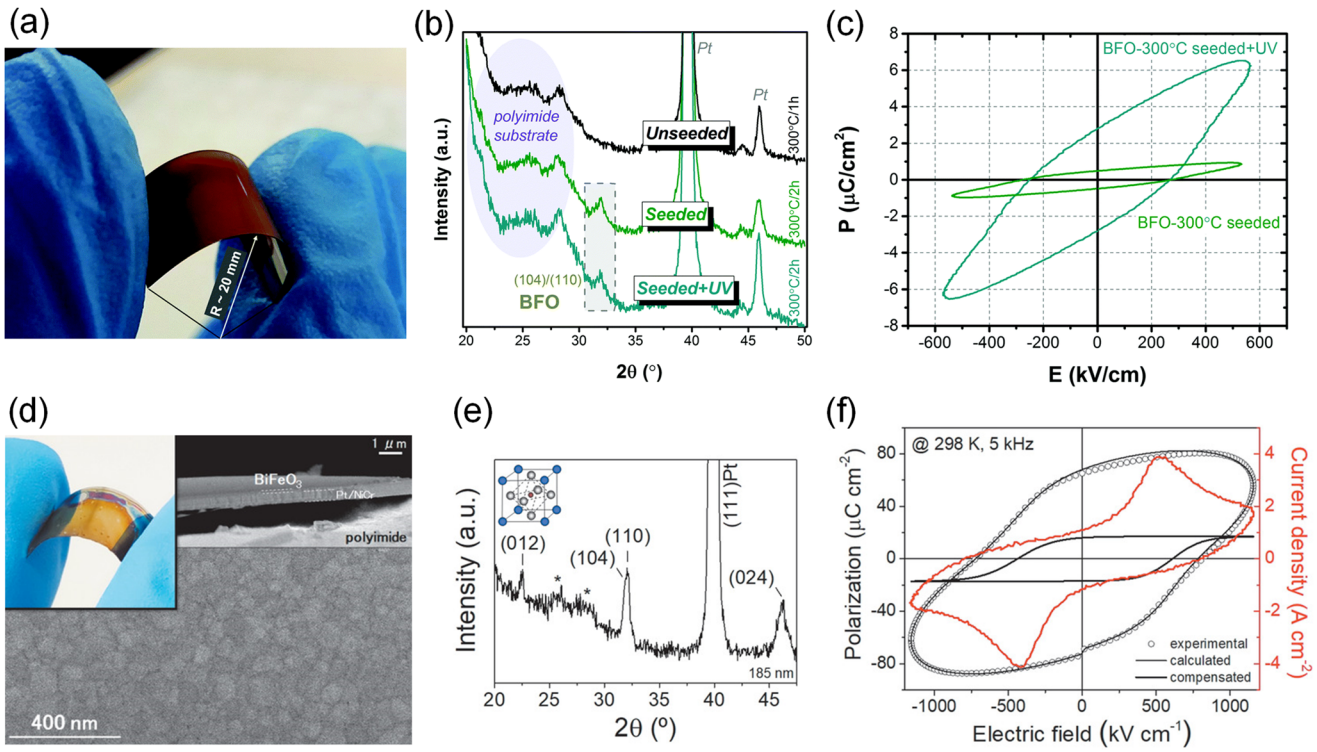

FIG. 16. (a) Photoimage of a seeded photosensitive precursor (SPP)-based $BiFeO_3$ (BFO) thin film fabricated on a flexible polyimide (PI) substrate: with bending radius, $R \sim 20$ mm. (b) XRD patterns of the BFO thin films processed at 300 °C on the PI substrate (*unseeded* films: amorphous phase; *seeded* and *seeded + UV* films: perovskite crystalline phase). (c) Ferroelectric hysteresis loops of the polarization–electric (*P–E*) field of the fabricated BFO thin films with seeded and seeded + UV condition with measuring conditions at 140 K and 10 kHz. Reproduced with permission from Tomczyk *et al.*, J. Mater. Chem. C **5**, 12529 (2017). Copyright 2017 Royal Society of Chemistry. (d) SEM images of the low-temperature processed BFO thin films annealed at 325 °C (inset: the flexible BFO thin film). (e) An XRD pattern of the flexible BFO thin film annealed at 325 °C on the Pt/Cr/Polyimide/NiCr/Pt substrate, (*: peaks from the substrate). (f) Ferroelectric hysteresis loops of *P–E* of the flexible BFO thin film prepared at 325 °C, measured at room temperature (298 K) and 5 kHz. Reproduced with permission from Bretos *et al.*, Adv. Funct. Mater. **30**, 2001897 (2020). Copyright 2020 John Wiley and Sons, Inc.

fabrication of the solution-derived BFO thin films on the flexible polyimide substrates [Figs. 16(d)–16(f)]. They proposed a novel "three-in-one" approach to decrease the crystallization temperature to form a perovskite phase of BFO below 350 °C: (1) the preparation of the photosensitive metal precursors with molecular complexes formed by metal cations (Bi or Fe) chelating with alkanolamine ligands (N-methydiehtanolamine, MDEA),[13] resembling the crystalline structures of oxide phase for chemical homogeneity; (2) UV-assisted photoannealing process[13,27] promoting photochemical reactions in the deposited precursor films leading to photochemical bond cleavage (i.e., photolysis), generation of reactive oxygen species, and further chemical reactions in M–O frameworks; and (3) internal combustion reactions[36] from the redox combination reactions between

TABLE IV. Parameters of HfO_2-based ferroelectric devices using the sol-gel metal oxide dielectric layer. (2,4-PD: 2,4-pentanedionate, Acac: acetylacetonate ligands, PrA: propionic acid, AcA: acetic acid, 2-ME: 2-methoxyethanol, EG: ethylene glycol solvent, ACN: acetonitrile solvent, Et-OH: ethanol, DIW: de-ionized water, *O*iPr: iso-propoxide, *t*-OiPr: tetra-iso-propoxide, and Y + Zr: Y-doped $HfZrO_2$ layer. *: Parameter was extracted from the data in the reconstructed graph; **FeFET: ferroelectric field-effect transistor.)

Year	Hf precursor	Solvent	Dopant	Dopant precursor	T_p (°C)	TE	Substrate (with BE)	d (nm)	P_r (μC/cm^2)	E_c (MV/cm)	Endurance test (cycle)
2014[199]	2,4-PD	PrA	Y	2,4-PD	700	Pt	Pt/TiO_2/SiO_2/Si	35	13	2.14	10^3
2015[200]	2,4-PD	PrA	Y Yb La Nd Sm Er	2,4-PD	800	Pt	Pt	45 42 42 42 42 42	20 ··· 12.7* 13.9* 12.3* 14.0*	1.4 ··· −1.07/+1.59* −1.38/+1.62* −1.09/+1.59* −1.27/+1.71*	···
2017[201]	2,4-PD	PrA	Al Ga In Mg Sr Ba Co/Ni	2,4-PD	800	Pt	Pt/TiO_2/SiO_2	42	3.0* 4.9* 5.3* 3.2* 12.9* 12.3* >3.7*	−0.80/+0.62* −0.91/+0.71* −1.32/+1.13* 0.79* −1.32/+1.57* −1.69/+1.45* ···	···
2017[202]	2,4-PD	PrA	Y	2,4-PD	800	TiN	Pt	15	10	−1.6/+1	10^5
2017[205]	O*i*Pr	2-ME	Zr	Nitrate	500	Pt	TiN/Si(100)	10	10	···	···
2017[206]	Chloride	Et-OH	Y	Chloride	800	···	Pt(111)/TiO_2/SiO_2/Si	9	20	1.4	···
2017[207]	*t*-O*i*Pr	2-ME	Zr	*t*-O*i*Pr	700	Pt	Pt(111)/TiO_2/Si(100)	40	2.1	0.58	···
2018[208]	*t*-O*i*Pr	2-ME	Zr	*t*-O*i*Pr	700	Pt	Pt(111)/TiO_2/Si(100)	40	8	0.8	···
2018[209]	Chloride	DIW	Y	Nitrate	700	TiN	*p*-type Si(100)	25	14.2	−1.45/+1.78	···
2018[210]	Chloride	Et-OH	Sr	Chloride	800	TiN	TiN/Si	···	1.51	2	10^7
2019[211]	2,4-PD	PrA	Sr	2,4-PD	700	Au	Pt/Ti/SiO_2/Si(100)	48.7	13.3	−1/+0.8	10^5
2019[212]	Chloride	DIW	Ca	Nitrate	700	TiN	*p*-type Si(100)	35	10.5	2	10^7
2019[213]	2,4-PD	AcA	Pr	Nitrate	800	Pt	Pt(111)/Ti/SiO_2/Si(111)	40	6.9	−1.1/+1.2	10^8
2020[188]	2,4-PD	AcA	Ce	Nitrate	800	Pt	*n*-type Si(100)	78	28.6	−1.2/+2.2	10^9
2020[214]	2,4-PD	PrA	···	···	700	TiN	TiN/Si(100)	136	22.56	···	>10^7
2020[215]	Acac	PrA	Y + Zr	Acac	800	Pt	Pt/Ti/SiO_2/Si	40	15	1.4	···
2020[216]	Acac	PrA	Y + Zr	Acac	800	Pt	Pt/Ti/SiO_2/Si	40	21	1.5	**FeTFT
2021[217]	Acac	PrA	Y + Zr	Acac	800	Pt/ITO	Pt/Ti/SiO_2/Si	13	10	1.3	**FeTFT
2021[218]	Chloride	EG, ACN	Zr	Chloride	450	Mo/AlOx	Mo/Glass	20	20	···	**FeTFT

oxidizing and reducing (fuel) agents from nitrate and MDEA to generate strong exothermic reactions (i.e., localized energy supply) in the precursor films at the lower phase conversion temperatures, promoting the complete decomposition of organic impurities and further reactions of oxide-formation.[24,26] Finally, the fabricated flexible BFO thin films through the three-in-one solution-based approach presented good ferroelectric performance (P_r ~ 17.5 $\mu C/cm^2$). Additionally, the flexible BFO thin films demonstrated good photocatalytic effects due to their relatively low bandgap (2.2–2.7 eV), which could open possibilities in the effective integration of photo-ferroelectrics in future electronic/energy applications.

B. Sol-gel hafnium dioxide films

This section reviews the recently highlighted sol-gel-based processing of ferroelectric oxide thin films of atomically doped hafnium oxide (doped-HfO_2), which has emerged as a new wave of ferroelectric materials research since the discovery of unconventional ferroelectric properties in 2011.[198] With regard to conventional ferroelectric materials, HfO_2-based ferroelectric thin films are advantageous owing to their wide bandgap, leading to efficient suppression of the gate leakage current and high compatibility with CMOS technology for large-scale integration.[185,189,198] In particular, we present a brief overview of the developments of sol-gel-derived ferroelectric doped-HfO_2 thin films with their research features and challenges over the past decade (Table IV).

In 2014, Starschich *et al.* presented ferroelectric HfO_2 films with yttrium (Y)[199,200] and different dopants of lanthanide groups, such as ytterbium (Yb), lanthanum (La), neodymium (Nd), samarium (Sm), and erbium (Er), with the same doping concentration[200] of 5.2 mol. % to investigate the phase formation and influence of the ferroelectric properties. Furthermore, they further studied HfO_2 films with very different dopants, such as magnesium (Mg with the ionic radii of 72 pm), strontium (Sr), and barium (Ba with the ionic radii of 135 pm) in terms of size, valence, and doping concentrations in the same film thickness of 42 nm.[201] The ionic radius of dopants larger than ~85 pm linearly affected the resulting ferroelectric performance with a higher P_r. Various alkaline earth metal ions induced the maximum P_r of the sol-gel-based HfO_2 films with a doping concentration of 7.5 mol. %, in contrast to the doping of the boron group (Al, Ga, and In) and rare earth metals with similar ionic radii (Co and Ni) with 5.2 mol. %. They also showed the importance of determining the failure mechanism of ferroelectric thin films via pulse measurements for the lifetime of ferroelectric memory devices, indicating that the lifetime is strongly related to pulse frequencies (Fig. 17).[202] The results of the wake-up effects of solution-derived Y-doped HfO_2 and the generation of oxygen vacancies at the interface of electrodes lead to the dielectric breakdown due to the high frequency of the pulsing bias.

The remnant polarization (P_r) is strongly correlated with the relative fractions of different crystalline phases in polycrystalline HfO_2, especially from a noncentrosymmetric orthorhombic (*o*-) phase (metastable) with the $Pbc2_1$ space group.[200,201] Therefore, the promotion of crystallization and stabilization of the *o*-phase, among the centrosymmetric phases [monoclinic (*m*-) at RT, tetragonal (*t*-), and cubic (*c*-) at higher temperatures][189] in HfO_2-based

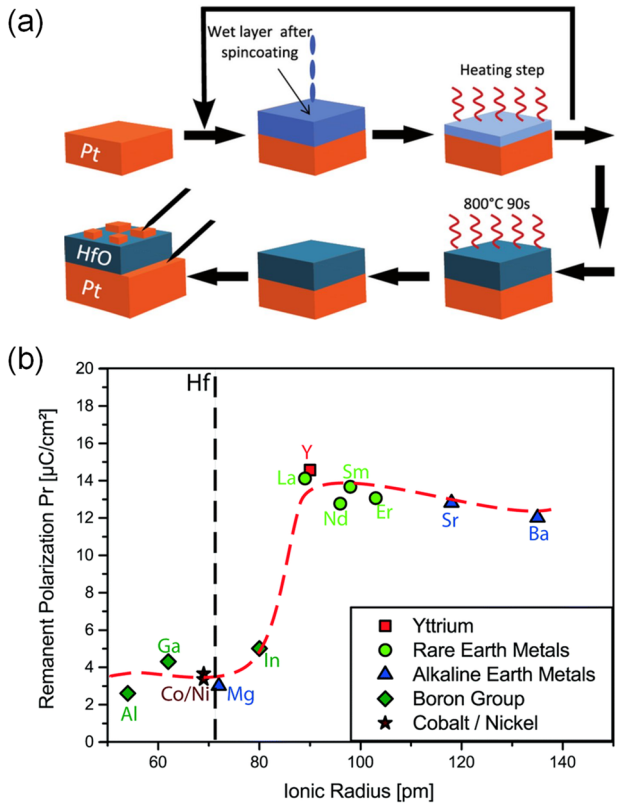

FIG. 17. (a) Schematic of the flow for the fabrication of the solution-processed ferroelectric HfO_2 thin film: loading the synthesized precursor solution with various metal dopants on the platinized (Pt) substrate, drying the as-spun films with soft-heating on a hot plate (with repeating for several times to obtain the desired thickness), annealing the film for crystallization at ~800 °C by a rapid thermal annealing process, and then depositing the top electrodes for MFM device structures. Reproduced with permission from Starschich *et al.*, ECS J. Solid State Sci. Technol. **4**, P419 (2015). Copyright 2015 IOP Publishing. (b) Distribution of remnant polarization (P_r) of solution-based HfO_2 ferroelectric devices with various dopants, including the different ionic radii, such as rare earth metals (Sm, Er, Nd, and La), alkaline earth metals (Mg, Sr, and Ba), boron group elements (In, Ga, and Al), and cobalt and nickel. Reproduced with permission from S. Starschich and U. Boettger, J. Mater. Chem. C **5**, 333 (2017). Copyright 2017 Royal Society of Chemistry.

films are vital for high-performance applications in ferroelectric memory devices. Zheng *et al.*[188] employed a four-valent dopant of Ce in sol-gel-derived HfO_2 on an n-type-doped silicon wafer substrate based on the preceding studies[203,204] of (1) theoretical calculations by first-principles computational investigation and (2) experimental results by physical vapor deposition on the epitaxial substrate, that is, the good solubility in the overall HfO_2 matrix and the preferred stabilization of the *o*-phase. They studied the microstructures and ferroelectric properties of CeO_2-HfO_2 solid solution thin films. With 15 mol. % of CeO_2 content, the doped HfO_2 ferroelectric films show the maximum value of P_r of 28.6 $\mu C/cm^2$ to 15 mol. % and good endurance behavior over 10^9 switching cycles (at 2.9 MV/cm with 100 kHz frequency), promising for sol-gel-based ferroelectric memory devices.

V. PHASE TRANSITION DEVICES

Recently, novel metal oxide materials have been intensively developed to overcome the physical limitations of the present Si technology (e.g., scaling issues and energy transfer loss). Since Mott's theory was reported in the 1940s,[219,220] the abrupt metal–insulator transition (MIT) behavior of the materials under external stimuli, such as various energy fields (e.g., thermal, electric, and magnetic), mechanical forces (e.g., strain, surface, and pressure), and photonic energies (e.g., visible, IR, and UV lights), can be interpreted as conventional phase transition types in metal oxides.

Mott insulators can be categorized into two major material classes: (1) the transition metal oxide group with a specific threshold temperature of MIT (T_{MIT}): VO_2 (T_{MIT} ~ 340 K),[221,222] NbO_2 (T_{MIT} ~ 1073 K),[223] Ca_2RuO_4 (T_{MIT} ~ 357 K),[224] and $ANiO_3$ (A = Pr, Nd) (T_{MIT} of 400–600 K),[225] and (2) the different metal chalcogenide crystal group of AM_4X_8 (A = Ga, Ge; M = V, Nb, Ta, Mo; and X = S, Se, Te) with low electric fields (<2 kV/cm) and/or hydrostatic pressures (GPa).[226,227]

Among the above Mott insulating materials, crystalline vanadium dioxide (VO_2) has attracted much attention in the V–O system due to the following properties: (i) T_{MIT} close to room temperature

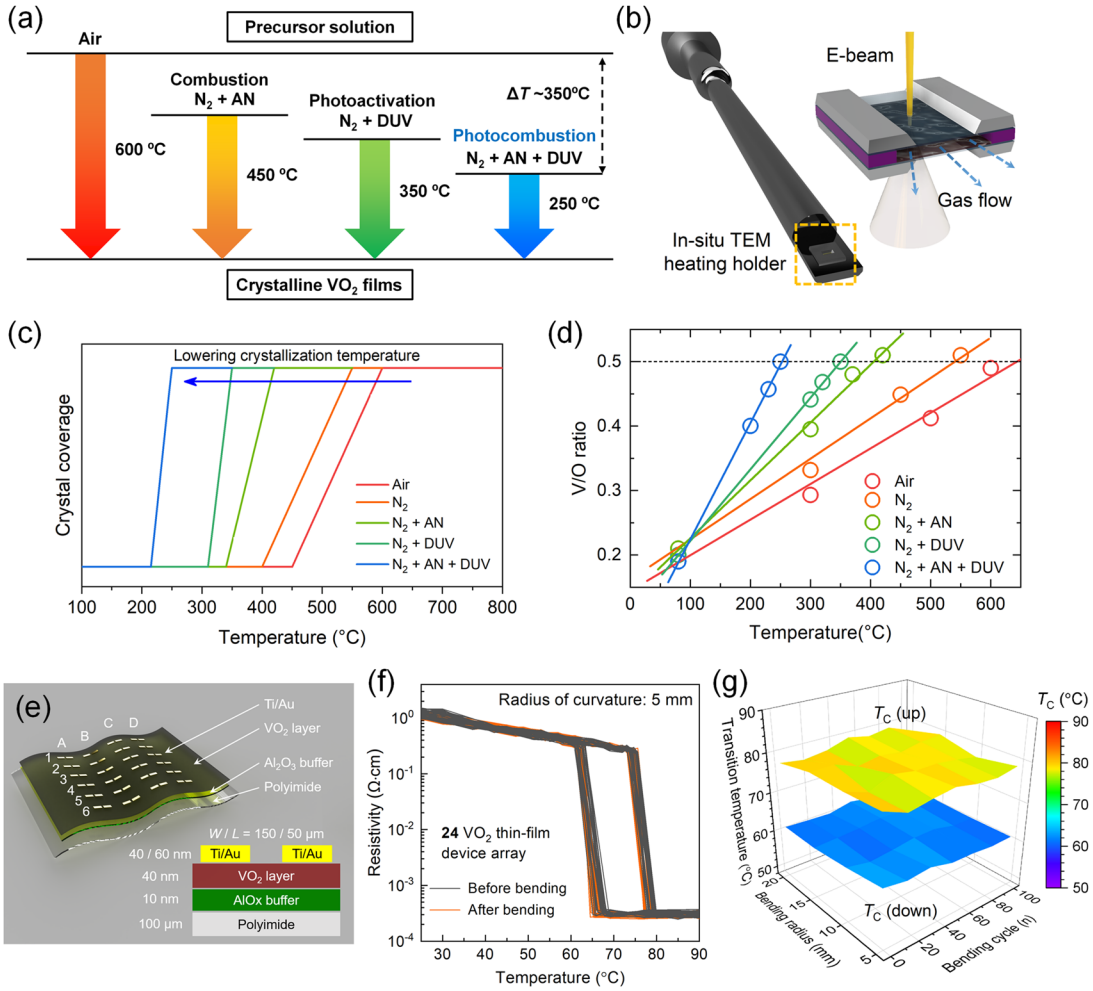

FIG. 18. (a) The processing temperatures required for forming crystalline VO_2 films from sol-gel precursor solutions under conventional (Air), combustion (N_2 + AN), photoactivation (N_2 + DUV), and photocombustion (N_2 + AN + DUV) conditions. (b) Illustration of an *in situ* gas flow TEM holder and its customized chip assembly for the morphological and structural analysis of VO_2 films from the different sol-gel precursor solutions. Schematic plots of the processing temperature-dependent (c) VO_2 crystalline coverage and (d) stoichiometric evolution of V/O ratio in VO_2 films prepared under the different sol-gel precursor conditions [from (c) *in situ* TEM and (d) TEM-EDS measurements of (b)]. (e) Illustration of the photocombusted VO_2 film directly grown on a flexible polyimide substrate with 24 device arrays (inset: the cross-sectional view of the fabricated VO_2 device structure). (f) Plots of resistivity vs temperature of the flexible 24 VO_2 device arrays before and after bending with the bending radius of 5 mm. (g) Statistical distributions of upward (yellow) and downward (blue) phase-transition temperatures as functions of the bending radius (5–20 mm) and bending cycles up to 100 cycles. Reproduced with permission from Jo *et al.*, Chem. Mater. **32**, 4013 (2020). Copyright 2020 American Chemical Society.

(340 K, ~67 °C), (ii) the reliable phase transition with a large change in electrical resistivity, and (iii) high transmittance in the visible light region.[222] The reversible and rapid resistivity change of VO_2 can be described as a first-order phase transition between a monoclinic (M) insulator phase (at low temperature) and a rutile (R) metallic phase (at high temperature). With interesting MIT behaviors, various types of applications, including Mott memristors,[228] data storages,[229,230] metamaterials,[230–232] bolometers,[233] smart-windows,[234] and strain, and gas-sensors,[235,236] have been demonstrated with advances in the fabrication strategies.

For the formation of the crystalline VO_2 phase, various deposition methods have been developed with relatively high processing temperatures: physical vapor deposition (at 450 °C)[237,238] and chemical vapor deposition (at 550 °C).[239] Such relatively high processing temperatures hinder the large area film uniformity and the choice of thermally weak plastic substrates. In addition to the vacuum process, the sol-gel derived VO_2 film formation has been widely explored for large-area and high throughput production, facile control of stoichiometry, and ease of tailoring device functionalities and performances by doping.[240–244] According to previous reports, however, the formation of the VO_2 film with the specific functionalities[13] from the sol-gel approach required a high annealing temperature above 600 °C[240–244] due to the hard to form crystalline lattice structure with strongly correlated electron systems (cf. additional key reviews[245,246] for solution-based VO_2 phase-transition devices).

Jo *et al.*[247] developed the novel photo-combustion process to significantly lower the formation temperature of the crystalline VO_2 phase from 600 to 250 °C by utilizing synergetic effects between solution combustion synthesis (SCS) and deep-UV (DUV) photoactivation. The sol-gel VO_2 precursor solutions were intermixed with ammonium nitrate (NH_4NO_3, AN) as a carbon-free oxidizing agent to promote an efficient exothermic combustive reaction with organic fuel agents [i.e., acetylacetonate (AcAcH)] and a photoactive radical generation via DUV photoactivation for efficient residual impurity removals and crystalline formation [Fig. 18(a)]. The crystallization kinetics of the prepared sol-gel VO_2 precursor solutions with five different conditions [(i) Air, (ii) N_2, (iii) N_2 + AN (combustion), (iv) N_2 + DUV (photoactivation), and (v) N_2+AN + DUV (photocombustion)] were carefully investigated by *in situ* gas heating transmission electron microscopy (TEM) with a temperature increase in every 10 °C [Fig. 18(b)]. Through the overall investigation of bright-field TEM images and selected-area electron diffractions, the conversion temperature from the amorphous and crystalline phase could be clearly distinguished under five (i)–(v) different conditions: the maximum temperatures of 450, 400, 340, 310, and 230 °C and the minimum temperatures of 600, 550, 420, 350, and 250 °C were indicated in Fig. 18(c) for the persistence of the amorphous regime and complete VO_2 crystalline coverage, respectively.

It is noted that the photocombustion conditions (v) of sol-gel VO_2 precursor solution films showed the lowest crystallization temperature of 250 °C compared to previous studies (30 cases) of sol-gel derived VO_2 films.[247] To further examine the dramatic reduction in VO_2 crystallization temperature via DUV photocombustion, the energy-dispersive x-ray spectroscopic (EDS) measurements were made to evaluate the V/O stoichiometric ratio of sol-gel VO_2 films [Fig. 18(d)]. The V/O ratio of 0.5 exhibits the completed conversion of crystalline VO_2 films (V:O = 1:2) after the oxygen reduction (i.e., oxygen vacancies), indicating a similar trend with the sharp slopes of crystal coverage (i.e., crystallization) in Fig. 18(c). For the first time, they demonstrated the sol-gel-based VO_2 flexible phase-transition device arrays (4 × 6 devices) on the plastic substrate due to large-area uniformity and reliable mechanical bendability by employing the DUV photocombustion process [Fig. 18(e)]. Under the reversible temperature changes, the first-order transition in stoichiometric VO_2 crystals has been successfully examined, along with the electrical resistive switching characteristic from the insulating (i.e., monoclinic phase) to the metallic state (i.e., rutile phase) with a hysteresis window. Finally, the phase-transition reliability and uniformity of the large-area VO_2 film on the flexible substrate were statistically characterized with 24 device arrays under bent conditions in Figs. 18(f) and 18(g). The statistical distributions of phase transition temperatures exhibit very narrow deviation within ±9% for the entire substrate area, regardless of severe reliability tests. Overall, the DUV-assisted photocombustion process can be applied to form large-area and flexible crystalline metal oxide materials for future electronics and energy devices with various functionalities with the evolution of a novel material-processing paradigm.

VI. CONCLUSION AND OUTLOOK

We have reviewed recent research advancements in solution-processed metal oxide dielectric materials. In comparison with our previous review,[4] this Research Update comprehensively covered the practical use of the dielectric layer in various electronics: (1) three-terminal-based devices such as a gate dielectric layer for field-effect transistors and (2) two-terminal-based devices, such as resistive, ferroelectric memory, and phase switching electronic devices. Unlike conventional vacuum-based deposition techniques, solution approaches (i.e., sol-gel precursor solution) can provide cost-efficient and large-area high-quality oxide dielectric materials. Furthermore, emerging low-temperature processes to compensate inevitable requirement of a high-thermal budget for oxide film condensation/densification/crystallization have been intensively studied over the past five years for the realization of proper electrical characteristics and reliability in the application of electronic devices. We have reviewed cutting-edge research approaches of the solution-processed metal oxide dielectric layer in a view of the following technical challenges: (1) low-temperature fabrication processes (even on flexible substrates), (2) large-area and high-throughput manufacturing processes, (3) creative design and strategy of solution synthesis and oxide composition, and (4) oxide structure formation (from amorphous to crystalline) for multi-functionalities.

For the further development of advanced electronic devices, studies on the low-temperature processes and large-area deposition/printing techniques of other functional electronic materials, such as semiconductor (e.g., carbon-based materials, metal organic framework, perovskite, organic small molecules, and liquid crystals), conductor (e.g., various metal alloys with various nanostructures or polymer conductors), and their formation onto suitable (flexible) substrates (e.g., engineering plastics and ultra-thin glasses), must be accompanied. The creative strategies of solution synthesis and designs of oxide composition will open the avenue for further

research studies on functional oxide dielectric materials. Through combinatorial composition to ternary and quaternary oxide systems, important clues can be found for developing novel materials with not only dielectric properties but also new physicochemical properties (e.g., simultaneous effects: both ferroelectrics and magnetic and/or photocatalytic effects). Comprehensive studies on (non-)stoichiometric oxide materials will also expand the use of solution-derived dielectric materials for various applications, such as energy storage, catalytic, and encapsulation layers. It is also necessary to further establish the reaction/formation mechanism of the crystallization pathway under various processing conditions with advanced characterization platforms (e.g., *in situ/operando* measurements of TEM/SEM/EDS/Raman),[13,247] beneficial to intentionally controlling of oxide functionalities based on the modulation of (i) the internal structure: crystal phases, grain size, strain and density, and crystal growth orientation, and (ii) surface/interfacial properties. The operational stability and reliable retention under external environmental conditions should be secured to have a quality guarantee close to that of the commercial Si and/or vacuum-processed oxide films. We hope that further research progress on solution-processed oxide dielectric films will pave the way for practical applications into next-generation IoT and future ubiquitous devices.

ACKNOWLEDGMENTS

This research was supported by the Korea Electric Power Corporation (Grant No. R21XO01-20) and research grants from the National Research Foundation of Korea (NRF) funded by the Ministry of Science and ICT, Korea (Grant Nos. NRF-2018M3A7B4070988, NRF-2020R1F1A1073564, NRF-2021R1A4A1033155, NRF-2020M3D1A1030660, NRF-2021R1A2C1013015 and NRF-2020M1A2A2080748). This work was also supported by the GIST Research Institute (GRI) grant funded by GIST in 2021.

AUTHOR DECLARATIONS

Conflict of Interest

The authors declare no competing financial interests.

Author Contributions

W.-J.L. and T.K. equally contributed to this work. All the authors discussed the contents and provided important contributions to the manuscript.

DATA AVAILABILITY

The data that support the findings of this study are available within the article.

REFERENCES

[1] L. L. Hench and J. K. West, Chem. Rev. **90**, 33 (1990).
[2] C. D. Chandler, C. Roger, and M. J. Hampden-Smith, Chem. Rev. **93**, 1205 (1993).
[3] C. J. Brinker and G. W. Scherer, *Sol–Gel Science: The Physics and Chemistry of Sol–Gel Processing* (Academic Press, 2013).
[4] S. Park, C.-H. Kim, W.-J. Lee, S. Sung, and M.-H. Yoon, Mater. Sci. Eng.: R Rep. **114**, 1 (2017).
[5] B. Wang, W. Huang, L. Chi, M. Al-Hashimi, T. J. Marks, and A. Facchetti, Chem. Rev. **118**, 5690 (2018).
[6] A. Liu, H. Zhu, H. Sun, Y. Xu, and Y.-Y. Noh, Adv. Mater. **30**, 1706364 (2018).
[7] J. W. Park, B. H. Kang, and H. J. Kim, Adv. Funct. Mater. **30**, 1904632 (2020).
[8] R. Chen and L. Lan, Nanotechnology **30**, 312001 (2019).
[9] W.-J. Lee, W.-T. Park, S. Park, S. Sung, Y.-Y. Noh, and M.-H. Yoon, Adv. Mater. **27**, 5043 (2015).
[10] E. Carlos, R. Branquinho, R. Martins, A. Kiazadeh, and E. Fortunato, Adv. Mater. **33**, 2004328 (2021).
[11] R. Waser, R. Dittmann, G. Staikov, and K. Szot, Adv. Mater. **21**, 2632 (2009).
[12] N. Bassiri-Gharb, Y. Bastani, and A. Bernal, Chem. Soc. Rev. **43**, 2125 (2014).
[13] I. Bretos, R. Jiménez, J. Ricote, and M. L. Calzada, Chem. Soc. Rev. **47**, 291 (2018).
[14] I. Bretos, R. Jimenez, J. Ricote, and M. L. Calzada, IEEE Trans. Ultrason. Ferroelectr. Freq. Control **67**, 1967 (2020).
[15] S. Yu, B. Gao, Z. Fang, H. Yu, J. Kang, and H.-S. P. Wong, Adv. Mater. **25**, 1774 (2013).
[16] K. Lu, X. Li, Q. Sun, X. Pang, J. Chen, T. Minari, X. Liu, and Y. Song, Mater. Horiz. **8**, 447 (2021).
[17] I. Burn and D. M. Smyth, J. Mater. Sci. **7**, 339 (1972).
[18] M. Osada and T. Sasaki, Adv. Mater. **24**, 210 (2012).
[19] P.-P. Shi, Y.-Y. Tang, P.-F. Li, W.-Q. Liao, Z.-X. Wang, Q. Ye, and R.-G. Xiong, Chem. Soc. Rev. **45**, 3811 (2016).
[20] J. F. Nye, *Physical Properties of Crystals: Their Representation by Tensors and Matrices* (Oxford University Press, 1985).
[21] M. Glazer, G. Burns, and A. N. Glazer, *Space Groups for Solid State Scientists* (Elsevier, 2012).
[22] Z. Wang, P. K. Nayak, J. A. Caraveo-Frescas, and H. N. Alshareef, Adv. Mater. **28**, 3831 (2016).
[23] A. Liu, H. Zhu, and Y.-Y. Noh, Mater. Sci. Eng.: R Rep. **135**, 85 (2019).
[24] P. Pujar, S. Gandla, D. Gupta, S. Kim, and M. G. Kim, Adv. Electron. Mater. **6**, 2000464 (2020).
[25] I. Bretos, R. Jiménez, J. Ricote, and M. L. Calzada, Chem. - Eur. J. **26**, 9277 (2020).
[26] E. Carlos, R. Martins, E. Fortunato, and R. Branquinho, Chem. - Eur. J. **26**, 9099 (2020).
[27] E. Yarali, C. Koutsiaki, H. Faber, K. Tetzner, E. Yengel, P. Patsalas, N. Kalfagiannis, D. C. Koutsogeorgis, and T. D. Anthopoulos, Adv. Funct. Mater. **30**, 1906022 (2020).
[28] J. W. Jo, S. H. Kang, J. S. Heo, Y. H. Kim, and S. K. Park, Chem. - Eur. J. **26**, 9126 (2020).
[29] I. Bretos, S. Diodati, R. Jiménez, F. Tajoli, J. Ricote, G. Bragaggia, M. Franca, M. L. Calzada, and S. Gross, Chem. - Eur. J. **26**, 9157 (2020).
[30] S. S. Shin, S. J. Lee, and S. I. Seok, Adv. Funct. Mater. **29**, 1900455 (2019).
[31] M. Parashar, V. K. Shukla, and R. Singh, J. Mater. Sci.: Mater. Electron. **31**, 3729 (2020).
[32] S. Alberti and J. Jágerská, Front. Mater. **8**, 629822 (2021).
[33] E. Carlos, R. Branquinho, R. Martins, and E. Fortunato, Solid-State Electron. **183**, 108044 (2021).
[34] S. Lee, S. H. Lee, N. On, and J. K. Jeong, Ceram. Int. **47**, 6918 (2021).
[35] X. Zhuang, S. Patel, C. Zhang, B. Wang, Y. Chen, H. Liu, V. P. Dravid, J. Yu, Y.-Y. Hu, W. Huang, A. Facchetti, and T. J. Marks, J. Am. Chem. Soc. **142**, 12440 (2020).
[36] A. Varma, A. S. Mukasyan, A. S. Rogachev, and K. V. Manukyan, Chem. Rev. **116**, 14493 (2016).
[37] M.-G. Kim, M. G. Kanatzidis, A. Facchetti, and T. J. Marks, Nat. Mater. **10**, 382 (2011).
[38] Y. Chen, B. Wang, W. Huang, X. Zhang, G. Wang, M. J. Leonardi, Y. Huang, Z. Lu, T. J. Marks, and A. Facchetti, Chem. Mater. **30**, 3323 (2018).

[39]B. Wang, M. J. Leonardi, W. Huang, Y. Chen, L. Zeng, B. J. Eckstein, T. J. Marks, and A. Facchetti, Adv. Electron. Mater. **5**, 1900540 (2019).
[40]B. Wang, P. Guo, L. Zeng, X. Yu, A. Sil, W. Huang, M. J. Leonardi, X. Zhang, G. Wang, S. Lu, Z. Chen, M. J. Bedzyk, R. D. Schaller, T. J. Marks, and A. Facchetti, Proc. Natl. Acad. Sci. U. S. A. **116**, 9230 (2019).
[41]F. Deganello and A. K. Tyagi, Prog. Cryst. Growth Charact. Mater. **64**, 23 (2018).
[42]N. Koslowski, R. C. Hoffmann, V. Trouillet, M. Bruns, S. Foro, and J. J. Schneider, RSC Adv. **9**, 31386 (2019).
[43]N. Koslowski, S. Sanctis, R. C. Hoffmann, M. Bruns, and J. J. Schneider, J. Mater. Chem. C **7**, 1048 (2019).
[44]N. Koslowski, V. Trouillet, and J. J. Schneider, J. Mater. Chem. C **8**, 8521 (2020).
[45]J.-W. Jo, Y.-H. Kim, J. Park, J. S. Heo, S. Hwang, W.-J. Lee, M.-H. Yoon, M.-G. Kim, and S. K. Park, ACS Appl. Mater. Interfaces **9**, 35114 (2017).
[46]G. F. Zou, J. Zhao, H. M. Luo, T. M. McCleskey, A. K. Burrell, and Q. X. Jia, Chem. Soc. Rev. **42**, 439 (2012).
[47]L. Chen, W. Xu, W. Liu, S. Han, P. Cao, M. Fang, D. Zhu, and Y. Lu, ACS Appl. Mater. Interfaces **11**, 29078 (2019).
[48]G. Park, H. Yang, J. H. Lee, G. Lee, J. Kwak, and U. Jeong, Adv. Mater. Interfaces **6**, 1900588 (2019).
[49]L. Yan, W. He, X. Liang, C. Liu, X. Lu, C. Luo, A. Zhang, R. Tao, Z. Fan, M. Zeng, H. Ning, G. Zhou, X. Lu, and J. Liu, J. Mater. Chem. C **8**, 5163 (2020).
[50]J. Chung, Y. J. Tak, W.-G. Kim, J. W. Park, T. S. Kim, J. H. Lim, and H. J. Kim, J. Mater. Chem. C **6**, 4928 (2018).
[51]F. Shao and Q. Wan, J. Phys. D: Appl. Phys. **52**, 143002 (2019).
[52]Y. Liang, J. Yong, Y. Yu, A. Nirmalathas, K. Ganesan, R. Evans, B. Nasr, and E. Skafidas, ACS Nano **13**, 13957 (2019).
[53]S. Hong, J. W. Na, I. S. Lee, H. T. Kim, B. H. Kang, J. Chung, and H. J. Kim, ACS Appl. Mater. Interfaces **12**, 39705 (2020).
[54]J. S. Heo, S.-P. Jeon, I. Kim, W. Lee, Y.-H. Kim, and S. K. Park, ACS Appl. Mater. Interfaces **11**, 48054 (2019).
[55]S.-P. Jeon, J. S. Heo, I. Kim, Y.-H. Kim, and S. K. Park, ACS Appl. Mater. Interfaces **12**, 57996 (2020).
[56]Y.-H. Kim, J.-S. Heo, T.-H. Kim, S. Park, M.-H. Yoon, J. Kim, M. S. Oh, G.-R. Yi, Y.-Y. Noh, and S. K. Park, Nature **489**, 128 (2012).
[57]S. Park, K.-H. Kim, J.-W. Jo, S. Sung, K.-T. Kim, W.-J. Lee, J. Kim, H. J. Kim, G.-R. Yi, Y.-H. Kim, M.-H. Yoon, and S. K. Park, Adv. Funct. Mater. **25**, 2807 (2015).
[58]J.-W. Jo, K.-H. Kim, J. Kim, S. G. Ban, Y.-H. Kim, and S. K. Park, ACS Appl. Mater. Interfaces **10**, 2679 (2018).
[59]W. J. Scheideler, M. W. McPhail, R. Kumar, J. Smith, and V. Subramanian, ACS Appl. Mater. Interfaces **10**, 37277 (2018).
[60]S. Bolat, P. Fuchs, S. Knobelspies, O. Temel, G. T. Sevilla, E. Gilshtein, C. Andres, I. Shorubalko, Y. Liu, G. Tröster, A. N. Tiwari, and Y. E. Romanyuk, Adv. Electron. Mater. **5**, 1800843 (2019).
[61]A. Mancinelli, S. Bolat, J. Kim, Y. E. Romanyuk, and D. Briand, ACS Appl. Electron. Mater. **2**, 3141 (2020).
[62]E. Yarali, H. Faber, E. Yengel, A. Seitkhan, K. Loganathan, G. T. Harrison, B. Adilbekova, Y. Lin, C. Ma, Y. Firdaus, and T. D. Anthopoulos, Adv. Electron. Mater. **6**, 2000028 (2020).
[63]T. B. Daunis, K. A. Schroder, and J. W. P. Hsu, npj Flexible Electron. **4**, 7 (2020).
[64]W.-J. Lee, J.-G. Choi, S. Sung, C.-H. Kim, S. Na, Y.-C. Joo, S. Park, and M.-H. Yoon, ACS Appl. Mater. Interfaces **13**, 2820 (2021).
[65]E. Carlos, R. Branquinho, A. Kiazadeh, J. Martins, P. Barquinha, R. Martins, and E. Fortunato, ACS Appl. Mater. Interfaces **9**, 40428 (2017).
[66]E. Carlos, J. Leppäniemi, A. Sneck, A. Alastalo, J. Deuermeier, R. Branquinho, R. Martins, and E. Fortunato, Adv. Electron. Mater. **6**, 1901071 (2020).
[67]E. Carlos, S. Dellis, N. Kalfagiannis, L. Koutsokeras, D. C. Koutsogeorgis, R. Branquinho, R. Martins, and E. Fortunato, J. Mater. Chem. C **8**, 6176 (2020).
[68]J. Lee, H. Seul, and J. K. Jeong, J. Alloys Compd. **741**, 1021 (2018).
[69]J. Kim, S. Choi, J.-W. Jo, S. K. Park, and Y.-H. Kim, Thin Solid Films **660**, 814 (2018).
[70]T. B. Daunis, J. M. H. Tran, and J. W. P. Hsu, ACS Appl. Mater. Interfaces **10**, 39435 (2018).
[71]J.-E. Huh, J. Park, J. Lee, S.-E. Lee, J. Lee, K.-H. Lim, and Y. S. Kim, J. Ind. Eng. Chem. **68**, 117 (2018).
[72]W. Wu, L. Liang, J. Yu, X. Xiao, H. Zhang, J. Gao, F. Zhuge, T.-C. Chang, L. Lan, and H. Cao, Ceram. Int. **45**, 15883 (2019).
[73]B.-S. Yu, J.-Y. Jeon, B.-C. Kang, W. Lee, Y.-H. Kim, and T.-J. Ha, Sci. Rep. **9**, 8416 (2019).
[74]S. Jana, E. Carlos, S. Panigrahi, R. Martins, and E. Fortunato, ACS Nano **14**, 14790 (2020).
[75]Z. Xin, Y. Ding, Y. Zhu, C. Fu, Z. Yao, Q. Chen, G. Liu, and F. Shan, Adv. Electron. Mater. **6**, 1901110 (2020).
[76]Q. Mu, Z. Chen, S. Duan, X. Zhang, X. Ren, and W. Hu, Front. Mater. **7**, 570002 (2020).
[77]Q. Liu, C. Zhao, I. Z. Mitrovic, W. Xu, L. Yang, and C. Z. Zhao, Adv. Electron. Mater. **6**, 2000072 (2020).
[78]J.-B. Seon, N.-K. Cho, G. Yoo, Y. S. Kim, and K. Char, RSC Adv. **8**, 39115 (2018).
[79]L. Zhu, G. He, W. Li, B. Yang, E. Fortunato, and R. Martins, Adv. Electron. Mater. **4**, 1800100 (2018).
[80]S. Wang and G. Xia, Ceram. Int. **45**, 23666 (2019).
[81]Y. Chen, X. Zhuang, E. A. Goldfine, V. P. Dravid, M. J. Bedzyk, W. Huang, A. Facchetti, and T. J. Marks, Adv. Funct. Mater. **30**, 2005069 (2020).
[82]S.-J. Park and T.-J. Ha, Thin Solid Films **708**, 138113 (2020).
[83]W. Huang, X. Yu, L. Zeng, B. Wang, A. Takai, G. Di Carlo, M. J. Bedzyk, T. J. Marks, and A. Facchetti, ACS Appl. Mater. Interfaces **13**, 3445 (2021).
[84]J. O. Kim, J. S. Hur, D. Kim, B. Lee, J. M. Jung, H. A. Kim, U. J. Chung, S. H. Nam, Y. Hong, K. S. Park, and J. K. Jeong, Adv. Funct. Mater. **30**, 1906647 (2020).
[85]S. H. Jung, H. S. Han, Y. B. Kim, D. S. Kim, N. G. Deshpande, S. J. Oh, J. H. Choi, and H. K. Cho, J. Alloys Compd. **847**, 156431 (2020).
[86]P. Pujar, K. K. Madaravalli Jagadeeshkumar, M. Naqi, S. Gandla, H. W. Cho, S. H. Jung, H. K. Cho, J. T. Kalathi, and S. Kim, ACS Appl. Mater. Interfaces **12**, 44926 (2020).
[87]C. Luo, T. Huang, C. Li, Y. Zhang, Z. Zou, Y. Li, R. Tao, J. Gao, G. Zhou, X. Lu, and J.-M. Liu, J. Phys. D: Appl. Phys. **54**, 125101 (2021).
[88]Z. Guo, A. Liu, Y. Meng, C. Fan, B. Shin, G. Liu, and F. Shan, Ceram. Int. **43**, 15194 (2017).
[89]M. Sharad, C. Augustine, G. Panagopoulos, and K. Roy, "Spin-based neuron model with domain-wall magnets as synapse," in *IEEE Transactions on Nanotechnology* (IEEE, 2012), Vol. 11, No. 4, pp. 843–853.
[90]Y. Zhang, J. Kang, O. Pluchery, L. Caillard, Y. J. Chabal, L.-W. Wang, J. F. Sanz, and M. Salmeron, ACS Appl. Nano Mater. **2**, 4711 (2019).
[91]M. P. West, P. Basnet, D. G. Pahinkar, R. H. Montgomery, S. Graham, and E. M. Vogel, Appl. Phys. Lett. **116**, 063504 (2020).
[92]F. Shao, Y. Yang, L. Q. Zhu, P. Feng, and Q. Wan, ACS Appl. Mater. Interfaces **8**, 3050 (2016).
[93]S. M. Kwon, S. W. Cho, M. Kim, J. S. Heo, Y. H. Kim, and S. K. Park, Adv. Mater. **31**, 1906433 (2019).
[94]X. Liang, Z. Li, L. Liu, S. Chen, X. Wang, and Y. Pei, Appl. Phys. Lett. **116**, 012102 (2020).
[95]S. Bolat, G. Torres Sevilla, A. Mancinelli, E. Gilshtein, J. Sastre, A. Cabas Vidani, D. Bachmann, I. Shorubalko, D. Briand, A. N. Tiwari, and Y. E. Romanyuk, Sci. Rep. **10**, 16664 (2020).
[96]Z. Y. Ren, L. Q. Zhu, L. Ai, X. Q. Lou, J. C. Cai, Z. Y. Li, and H. Xiao, J. Mater. Sci. **56**, 4316 (2021).
[97]A. Polsky, B. W. Mel, and J. Schiller, Nat. Neurosci. **7**, 621 (2004).
[98]L. Guo, Q. Wan, C. Wan, L. Zhu, and Y. Shi, IEEE Electron Device Lett. **34**, 1581 (2013).
[99]D. E. Feldman, Neuron **75**, 556 (2012).
[100]F. Idrees, J. Hou, C. Cao, F. K. Butt, I. Shakir, M. Tahir, and F. Idrees, Electrochim. Acta **216**, 332 (2016).
[101]H. Ling, D. A. Koutsouras, S. Kazemzadeh, Y. van de Burgt, F. Yan, and P. Gkoupidenis, Appl. Phys. Rev. **7**, 011307 (2020).
[102]S. Dai, Y. Zhao, Y. Wang, J. Zhang, L. Fang, S. Jin, Y. Shao, and J. Huang, Adv. Funct. Mater. **29**, 1903700 (2019).
[103]K. Qian, V. C. Nguyen, T. Chen, and P. S. Lee, J. Mater. Chem. C **4**, 9637 (2016).

[104]G. H. Kim, J. H. Lee, Y. Ahn, W. Jeon, S. J. Song, J. Y. Seok, J. H. Yoon, K. J. Yoon, T. J. Park, and C. S. Hwang, Adv. Funct. Mater. **23**, 1440 (2013).
[105]B. J. Choi, D. S. Jeong, S. K. Kim, C. Rohde, S. Choi, J. H. Oh, H. J. Kim, C. S. Hwang, K. Szot, R. Waser, B. Reichenberg, and S. Tiedke, J. Appl. Phys. **98**, 033715 (2005).
[106]J. H. Yoon, S. J. Song, I.-H. Yoo, J. Y. Seok, K. J. Yoon, D. E. Kwon, T. H. Park, and C. S. Hwang, Adv. Funct. Mater. **24**, 5086 (2014).
[107]F. Rahman, T. Ahmed, S. Walia, E. Mayes, S. Sriram, M. Bhaskaran, and S. Balendhran, Nanoscale **10**, 19711 (2018).
[108]B. W. Fowler, Y.-F. Chang, F. Zhou, Y. Wang, P.-Y. Chen, F. Xue, Y.-T. Chen, B. Bringhurst, S. Pozder, and J. C. Lee, RSC Adv. **5**, 21215 (2015).
[109]D.-H. Kwon, K. M. Kim, J. H. Jang, J. M. Jeon, M. H. Lee, G. H. Kim, X.-S. Li, G.-S. Park, B. Lee, S. Han, M. Kim, and C. S. Hwang, Nat. Nanotechnol. **5**, 148 (2010).
[110]A. A. Ogwu and T. H. Darma, J. Appl. Phys. **113**, 183522 (2013).
[111]A. Sawa, Mater. Today **11**, 28 (2008).
[112]F. Pan, S. Gao, C. Chen, C. Song, and F. Zeng, Mater. Sci. Eng.: R Rep. **83**, 1 (2014).
[113]S.-T. Han, Y. Zhou, and V. A. L. Roy, Adv. Mater. **25**, 5425 (2013).
[114]S. Gao, X. Yi, J. Shang, G. Liu, and R.-W. Li, Chem. Soc. Rev. **48**, 1531 (2019).
[115]H.-L. Yuan and J.-C. Li, J. Alloys Compd. **709**, 752 (2017).
[116]S.-J. Kim, H. Lee, and S.-H. Hong, Solid-State Electron. **142**, 56 (2018).
[117]J. Chu, Y. Li, X. Fan, H. Shao, W. Duan, and Y. Pei, Semicond. Sci. Technol. **33**, 115007 (2018).
[118]Y. Li, J. Chu, W. Duan, G. Cai, X. Fan, X. Wang, G. Wang, and Y. Pei, ACS Appl. Mater. Interfaces **10**, 24598 (2018).
[119]J.-C. Li, H.-P. Cui, and X.-Y. Hou, J. Alloys Compd. **752**, 247 (2018).
[120]H.-W. Yun, H. K. Woo, S. J. Oh, and S.-H. Hong, Curr. Appl. Phys. **20**, 288 (2020).
[121]V. Prusakova, C. Collini, M. Nardi, R. Tatti, L. Lunelli, L. Vanzetti, L. Lorenzelli, G. Baldi, A. Chiappini, A. Chiasera, D. Ristic, R. Verucchi, M. Bortolotti, and S. Dirè, RSC Adv. **7**, 1654 (2017).
[122]Y. Yu, F. Yang, S. Mao, S. Zhu, Y. Jia, L. Yuan, M. Salmen, and B. Sun, Chem. Phys. Lett. **706**, 477 (2018).
[123]V. Aglieri, A. Zaffora, G. Lullo, M. Santamaria, F. Di Franco, U. Lo Cicero, M. Mosca, and R. Macaluso, Superlattices Microstruct. **113**, 135 (2018).
[124]S. Chen, S. Noori, M. A. Villena, Y. Shi, T. Han, Y. Zuo, M. Pedeferri, D. Strukov, M. Lanza, and M. V. Diamanti, Chem. Mater. **31**, 8394 (2019).
[125]L. Zou, Curr. Appl. Phys. **24**, 32 (2021).
[126]C.-C. Hsu, J.-K. Sun, C.-C. Tsao, and P.-Y. Chuang, Physica B **519**, 21 (2017).
[127]G. Vescio, A. Crespo-Yepes, D. Alonso, S. Claramunt, M. Porti, R. Rodriguez, A. Cornet, A. Cirera, M. Nafria, and X. Aymerich, IEEE Electron Device Lett. **38**, 457 (2017).
[128]C.-C. Hsu, J.-K. Sun, C.-C. Tsao, and Y.-T. Chen, Physica B **508**, 98 (2017).
[129]J. Wang, S. Choudhary, J. De Roo, K. De Keukeleere, I. Van Driessche, A. J. Crosby, and S. S. Nonnenmann, ACS Appl. Mater. Interfaces **10**, 4824 (2018).
[130]A. Zaffora, R. Macaluso, H. Habazaki, I. Valov, and M. Santamaria, Electrochim. Acta **274**, 103 (2018).
[131]A. Zaffora, F. Di Quarto, H. Habazaki, I. Valov, and M. Santamaria, Faraday Discuss. **213**, 165 (2019).
[132]I. Zrinski, C. C. Mardare, L.-I. Jinga, J. P. Kollender, G. Socol, A. W. Hassel, and A. I. Mardare, Appl. Surf. Sci. **548**, 149093 (2021).
[133]J. Jang and V. Subramanian, Thin Solid Films **625**, 87 (2017).
[134]L. Li, Y. Chen, X. Yin, Y. Song, N. Li, J. Niu, H. Wu, and W. Qu, Nanotechnology **28**, 485707 (2017).
[135]W.-Y. Jian, H.-C. You, and C.-Y. Wu, Jpn. J. Appl. Phys., Part 1 **57**, 011501 (2017).
[136]C.-C. Hsu, T.-C. Wang, and C.-C. Tsao, J. Alloys Compd. **769**, 65 (2018).
[137]S.-J. Park, B.-S. Yu, J.-Y. Jeon, B.-C. Kang, and T.-J. Ha, J. Alloys Compd. **825**, 154086 (2020).
[138]S.-T. Kim and W.-J. Cho, Semicond. Sci. Technol. **33**, 015009 (2017).
[139]M.-S. Kang and W.-J. Cho, J. Phys. Chem. Solids **123**, 52 (2018).
[140]E. Carlos, A. Kiazadeh, J. Deuermeier, R. Branquinho, R. Martins, and E. Fortunato, Nanotechnology **29**, 345206 (2018).
[141]W. Zhang, Y. Mao, and W. Duan, Phys. Status Solidi RRL **13**, 1900016 (2019).
[142]W. Duan, Mater. Res. Express **6**, 115923 (2019).
[143]Y. Qi, C. Zhao, C. Z. Zhao, W. Xu, Z. Shen, J. He, T. Zhao, Y. Fang, Q. Liu, R. Yi, and L. Yang, Solid-State Electron. **158**, 28 (2019).
[144]Y. Qi, Z. Shen, C. Zhao, and C. Z. Zhao, J. Alloys Compd. **822**, 153603 (2020).
[145]E. Carlos, J. Deuermeier, R. Branquinho, C. Gaspar, R. Martins, A. Kiazadeh, and E. Fortunato, J. Mater. Chem. C **9**, 3911 (2021).
[146]C. Yao, M. Ismail, A. Hao, S. K. Thatikonda, W. Huang, N. Qin, and D. Bao, RSC Adv. **9**, 12615 (2019).
[147]C. Yao, W. Hu, M. Ismail, S. K. Thatikonda, A. Hao, S. He, N. Qin, W. Huang, and D. Bao, Curr. Appl. Phys. **19**, 1286 (2019).
[148]C. Yao, M. Ismail, A. Hao, T. S. Kumar, W. Huang, N. Qin, and D. Bao, Phys. Status Solidi RRL **13**, 1900168 (2019).
[149]A. Zaffora, D.-Y. Cho, K.-S. Lee, F. Di Quarto, R. Waser, M. Santamaria, and I. Valov, Adv. Mater. **29**, 1703357 (2017).
[150]M. Sophocleous, N. Mohammadian, L. A. Majewski, and J. Georgiou, Mater. Lett. **269**, 127676 (2020).
[151]R. Chen, W. Hu, L. Zou, Y. Ke, A. Hao, and D. Bao, Curr. Appl. Phys. **19**, 987 (2019).
[152]P. Li, D. Wang, Z. Zhang, Y. Guo, L. Jiang, and C. Xu, ACS Appl. Mater. Interfaces **12**, 56186 (2020).
[153]A. Thakre, J. Kaswan, A. K. Shukla, and A. Kumar, RSC Adv. **7**, 54111 (2017).
[154]K.-J. Lee, Y.-C. Chang, C.-J. Lee, L.-W. Wang, D.-W. Chou, T.-K. Chiang, and Y.-H. Wang, IEEE Trans. Electron Devices **64**, 2001 (2017).
[155]A. Thakre and A. Kumar, Vacuum **151**, 182 (2018).
[156]S. Lee, S. Kwak, T. Park, B. Son, H. J. Yun, J. Hur, and H. Yoo, Molecules **26**, 5446 (2021).
[157]L.-Q. Wang, W.-H. Li, X.-G. Tang, X.-B. Guo, Q.-X. Liu, Y.-P. Jiang, and Z.-H. Tang, Ceram. Int. **47**, 5617 (2021).
[158]Z. Miao, L. Chen, F. Zhou, and Q. Wang, J. Phys. D: Appl. Phys. **51**, 025107 (2017).
[159]A. Thakre and A. Kumar, AIP Adv. **7**, 125115 (2017).
[160]A. Hao, S. He, N. Qin, R. Chen, and D. Bao, Ceram. Int. **43**, S481 (2017).
[161]A. Hao, M. Ismail, S. He, N. Qin, R. Chen, A. M. Rana, and D. Bao, Mater. Sci. Eng.: B **229**, 86 (2018).
[162]A. Hao, D. Jia, M. Ismail, W. Huang, R. Chen, and D. Bao, Appl. Phys. Lett. **114**, 203502 (2019).
[163]C. Yao, A. Hao, S. K. Thatikonda, W. Huang, N. Qin, and D. Bao, Thin Solid Films **699**, 137889 (2020).
[164]C. Kumari, I. Varun, S. Prakash Tiwari, and A. Dixit, Superlattices Microstruct. **120**, 67 (2018).
[165]A. K. Jena, S. Satapathy, and J. Mohanty, Phys. Chem. Chem. Phys. **21**, 15854 (2019).
[166]I. Kim, M. Siddik, J. Shin, K. P. Biju, S. Jung, and H. Hwang, Appl. Phys. Lett. **99**, 042101 (2011).
[167]G. Chen, C. Song, C. Chen, S. Gao, F. Zeng, and F. Pan, Adv. Mater. **24**, 3515 (2012).
[168]T. Guo, T. Tan, and Z. Liu, Appl. Surf. Sci. **351**, 704 (2015).
[169]T. Tan, T. Guo, and Z. Liu, J. Alloys Compd. **610**, 388 (2014).
[170]A. Hao, M. Ismail, S. He, N. Qin, W. Huang, J. Wu, and D. Bao, RSC Adv. **7**, 46665 (2017).
[171]Q. Liu, S. Long, H. Lv, W. Wang, J. Niu, Z. Huo, J. Chen, and M. Liu, ACS Nano **4**, 6162 (2010).
[172]T. Guo, T. Tan, Z. Liu, and B. Liu, J. Alloys Compd. **686**, 669 (2016).
[173]Z. Yue, G. Tan, H. Ren, A. Xia, D. Shao, M. Guo, W. Yang, and Z. Chai, ACS Appl. Mater. Interfaces **9**, 20205 (2017).
[174]W. Hu, N. Qin, G. Wu, Y. Lin, S. Li, and D. Bao, J. Am. Chem. Soc. **134**, 14658 (2012).
[175]S. Munjal and N. Khare, Appl. Phys. Lett. **113**, 243501 (2018).

[176]A. Hao, M. Ismail, S. He, N. Qin, W. Huang, J. Wu, and D. Bao, J. Alloys Compd. **732**, 573 (2018).
[177]C. Baeumer, N. Raab, T. Menke, C. Schmitz, R. Rosezin, P. Müller, M. Andrä, V. Feyer, R. Bruchhaus, F. Gunkel, C. M. Schneider, R. Waser, and R. Dittmann, Nanoscale **8**, 13967 (2016).
[178]M. Uenuma, Y. Ishikawa, and Y. Uraoka, Appl. Phys. Lett. **107**, 073503 (2015).
[179]N. Birks, G. H. Meier, and F. S. Pettit, *Introduction to the High Temperature Oxidation of Metals* (Cambridge University Press, 2006).
[180]D. R. Lide, *CRC Handbook of Chemistry and Physics*, 77th ed. (CRC, Boca Raton, 1996).
[181]T. B. Reed, *Free Energy of Formation of Binary Compounds* (MIT Press, 1971).
[182]Z. B. Yan and J.-M. Liu, Ann. Phys. **358**, 206 (2015).
[183]F. Zahoor, T. Z. Azni Zulkifli, and F. A. Khanday, Nanoscale Res. Lett. **15**, 90 (2020).
[184]Y. Chen, L. Li, X. Yin, A. Yerramilli, Y. Shen, Y. Song, W. Bian, N. Li, Z. Zhao, W. Qu, N. D. Theodore, and T. L. Alford, IEEE Electron Device Lett. **38**, 1528 (2017).
[185]M. H. Park, Y. H. Lee, T. Mikolajick, U. Schroeder, and C. S. Hwang, MRS Commun. **8**, 795 (2018).
[186]M. H. Park, D. H. Lee, K. Yang, J.-Y. Park, G. T. Yu, H. W. Park, M. Materano, T. Mittmann, P. D. Lomenzo, T. Mikolajick, U. Schroeder, and C. S. Hwang, J. Mater. Chem. C **8**, 10526 (2020).
[187]J. F. Scott, *Ferroelectric Memories*, 1st ed. (Springer-Verlag, Berlin, Heidelberg, 2000).
[188]S. Zheng, Z. Zhao, Z. Liu, B. Zeng, L. Yin, Q. Peng, M. Liao, and Y. Zhou, Appl. Phys. Lett. **117**, 212904 (2020).
[189]M. H. Park, Y. H. Lee, H. J. Kim, Y. J. Kim, T. Moon, K. D. Kim, J. Müller, A. Kersch, U. Schroeder, T. Mikolajick, and C. S. Hwang, Adv. Mater. **27**, 1811 (2015).
[190]B. Yang, L. Jin, R. Wei, X. Tang, L. Hu, P. Tong, J. Yang, W. Song, J. Dai, X. Zhu, Y. Sun, S. Zhang, X. Wang, and Z. Cheng, Small **17**, 1903663 (2021).
[191]Q. Zhang, D. Sando, and V. Nagarajan, J. Mater. Chem. C **4**, 4092 (2016).
[192]C. Liu, F. An, P. S. M. Gharavi, Q. Lu, J. Zha, C. Chen, L. Wang, X. Zhan, Z. Xu, Y. Zhang, K. Qu, J. Yao, Y. Ou, Z. Zhao, X. Zhong, D. Zhang, N. Valanoor, L. Chen, T. Zhu, D. Chen, X. Zhai, P. Gao, T. Jia, S. Xie, G. Zhong, and J. Li, Natl. Sci. Rev. **7**, 84 (2020).
[193]Q. Zhang, H.-H. Huang, D. Sando, M. Summers, P. Munroe, O. Standard, and N. Valanoor, J. Mater. Chem. C **6**, 2882 (2018).
[194]J. M. Vila-Fungueiriño, A. Gómez, J. Antoja-Lleonart, J. Gázquez, C. Magén, B. Noheda, and A. Carretero-Genevrier, Nanoscale **10**, 20155 (2018).
[195]Q. Zhang, A. Rana, X. Liu, and N. Valanoor, ACS Appl. Electron. Mater. **1**, 154 (2019).
[196]M. Tomczyk, I. Bretos, R. Jiménez, A. Mahajan, E. V. Ramana, M. L. Calzada, and P. M. Vilarinho, J. Mater. Chem. C **5**, 12529 (2017).
[197]I. Bretos, R. Jiménez, J. Ricote, R. Sirera, and M. L. Calzada, Adv. Funct. Mater. **30**, 2001897 (2020).
[198]T. S. Böscke, J. Müller, D. Bräuhaus, U. Schröder, and U. Böttger, Appl. Phys. Lett. **99**, 102903 (2011).
[199]S. Starschich, D. Griesche, T. Schneller, R. Waser, and U. Böttger, Appl. Phys. Lett. **104**, 202903 (2014).
[200]S. Starschich, D. Griesche, T. Schneller, and U. Böttger, ECS J. Solid State Sci. Technol. **4**, P419 (2015).
[201]S. Starschich and U. Boettger, J. Mater. Chem. C **5**, 333 (2017).
[202]S. Starschich, S. Menzel, and U. Böttger, J. Appl. Phys. **121**, 154102 (2017).
[203]C. Künneth, R. Materlik, M. Falkowski, and A. Kersch, ACS Appl. Nano Mater. **1**, 254 (2018).
[204]T. Shiraishi, S. Choi, T. Kiguchi, T. Shimizu, H. Funakubo, and T. J. Konno, Appl. Phys. Lett. **114**, 232902 (2019).
[205]J. Y. Lee, G. Anoop, H. J. Lee, J. H. Kwak, and J. Y. Jo, Curr. Appl. Phys. **17**, 704 (2017).
[206]S. Kim and J. Hong, Ceram. Int. **43**, S158 (2017).
[207]C. Abe, S. Nakayama, M. Shiokawa, H. Kawashima, K. Katayama, T. Shiraishi, T. Shimizu, H. Funakubo, and H. Uchida, Ceram. Int. **43**, S501 (2017).
[208]S. Nakayama, H. Funakubo, and H. Uchida, Jpn. J. Appl. Phys., Part 1 **57**, 11UF06 (2018).
[209]X. Wang, D. Zhou, S. Li, X. Liu, P. Zhao, N. Sun, F. Ali, and J. Wang, Ceram. Int. **44**, 13867 (2018).
[210]A. Wei, C. Chen, L. Tang, K. Zhou, and D. Zhang, J. Alloys Compd. **731**, 546 (2018).
[211]L. Tang, C. Chen, A. Wei, K. Li, D. Zhang, and K. Zhou, Ceram. Int. **45**, 3140 (2019).
[212]Y. Yao, D. Zhou, S. Li, J. Wang, N. Sun, F. Liu, and X. Zhao, J. Appl. Phys. **126**, 154103 (2019).
[213]H. Liu, S. Zheng, Q. Chen, B. Zeng, J. Jiang, Q. Peng, M. Liao, and Y. Zhou, J. Mater. Sci.: Mater. Electron. **30**, 5771 (2019).
[214]H. Chen, Y. Chen, L. Tang, H. Luo, K. Zhou, X. Yuan, and D. Zhang, J. Mater. Chem. C **8**, 2820 (2020).
[215]Mohit, T. M. Murakami, K.-i. Haga, and E. Tokumitsu, Jpn. J. Appl. Phys., Part 1 **59**, SPPB03 (2020).
[216]Mohit, K.-i. Haga, and E. Tokumitsu, Jpn. J. Appl. Phys., Part 1 **59**, SMMB02 (2020).
[217]Mohit, T. Miyasako, and E. Tokumitsu, Jpn. J. Appl. Phys., Part 1 **60**, SBBM02 (2021).
[218]M. M. Hasan, C. W. Ahn, T. H. Kim, and J. Jang, Appl. Phys. Lett. **118**, 152901 (2021).
[219]N. Mott, *Metal-Insulator Transitions* (CRC Press, 2004).
[220]M. Imada, A. Fujimori, and Y. Tokura, Rev. Mod. Phys. **70**, 1039 (1998).
[221]J. Kim, C. Ko, A. Frenzel, S. Ramanathan, and J. E. Hoffman, Appl. Phys. Lett. **96**, 213106 (2010).
[222]F. J. Morin, Phys. Rev. Lett. **3**, 34 (1959).
[223]F. A. Chudnovskii, L. L. Odynets, A. L. Pergament, and G. B. Stefanovich, J. Solid State Chem. **122**, 95 (1996).
[224]C. S. Alexander, G. Cao, V. Dobrosavljevic, S. McCall, J. E. Crow, E. Lochner, and R. P. Guertin, Phys. Rev. B **60**, R8422 (1999).
[225]H. Park, A. J. Millis, and C. A. Marianetti, Phys. Rev. Lett. **109**, 156402 (2012).
[226]L. Cario, C. Vaju, B. Corraze, V. Guiot, and E. Janod, Adv. Mater. **22**, 5193 (2010).
[227]E. Janod, J. Tranchant, B. Corraze, M. Querré, P. Stoliar, M. Rozenberg, T. Cren, D. Roditchev, V. T. Phuoc, M.-P. Besland, and L. Cario, Adv. Funct. Mater. **25**, 6287 (2015).
[228]T. Driscoll, H.-T. Kim, B.-G. Chae, M. Di Ventra, and D. N. Basov, Appl. Phys. Lett. **95**, 043503 (2009).
[229]M.-J. Lee, Y. Park, D.-S. Suh, E.-H. Lee, S. Seo, D.-C. Kim, R. Jung, B.-S. Kang, S.-E. Ahn, C. B. Lee, D. H. Seo, Y.-K. Cha, I.-K. Yoo, J.-S. Kim, and B. H. Park, Adv. Mater. **19**, 3919 (2007).
[230]T. Driscoll, H.-T. Kim, B.-G. Chae, B.-J. Kim, Y.-W. Lee, N. M. Jokerst, S. Palit, D. R. Smith, M. Di Ventra, and D. N. Basov, Science **325**, 1518 (2009).
[231]T. Driscoll, S. Palit, M. M. Qazilbash, M. Brehm, F. Keilmann, B.-G. Chae, S.-J. Yun, H.-T. Kim, S. Y. Cho, N. M. Jokerst, D. R. Smith, and D. N. Basov, Appl. Phys. Lett. **93**, 024101 (2008).
[232]C. Zhang, G. Zhou, J. Wu, Y. Tang, Q. Wen, S. Li, J. Han, B. Jin, J. Chen, and P. Wu, Phys. Rev. Appl. **11**, 054016 (2019).
[233]C. Chen, X. Yi, X. Zhao, and B. Xiong, Sens. Actuators, A **90**, 212 (2001).
[234]Y. Gao, H. Luo, Z. Zhang, L. Kang, Z. Chen, J. Du, M. Kanehira, and C. Cao, Nano Energy **1**, 221 (2012).
[235]B. Hu, Y. Ding, W. Chen, D. Kulkarni, Y. Shen, V. V. Tsukruk, and Z. L. Wang, Adv. Mater. **22**, 5134 (2010).
[236]E. Strelcov, Y. Lilach, and A. Kolmakov, Nano Lett. **9**, 2322 (2009).
[237]H. Y. Xu, Y. H. Huang, S. Liu, K. W. Xu, F. Ma, and P. K. Chu, RSC Adv. **6**, 79383 (2016).
[238]S. Long, X. Cao, R. Huang, F. Xu, N. Li, A. Huang, G. Sun, S. Bao, H. Luo, and P. Jin, ACS Appl. Mater. Interfaces **11**, 22692 (2019).
[239]M. B. Sahana, G. N. Subbanna, and S. A. Shivashankar, J. Appl. Phys. **92**, 6495 (2002).

[240]J. Ye, L. Zhou, F. Liu, J. Qi, W. Gong, Y. Lin, and G. Ning, J. Alloys Compd. **504**, 503 (2010).
[241]Z. Zhang, Y. Gao, Z. Chen, J. Du, C. Cao, L. Kang, and H. Luo, Langmuir **26**, 10738 (2010).
[242]O. Berezina, D. Kirienko, A. Pergament, G. Stefanovich, A. Velichko, and V. Zlomanov, Thin Solid Films **574**, 15 (2015).
[243]M. E. A. Warwick and R. Binions, J. Mater. Chem. A **2**, 3275 (2014).
[244]N. Wang, N. T. Chew Shun, M. Duchamp, R. E. Dunin-Borkowski, Z. Li, and Y. Long, RSC Adv. **6**, 48455 (2016).
[245]S. Wang, M. Liu, L. Kong, Y. Long, X. Jiang, and A. Yu, Prog. Mater. Sci. **81**, 1 (2016).
[246]V. Devthade and S. Lee, J. Appl. Phys. **128**, 231101 (2020).
[247]Y.-R. Jo, W.-J. Lee, M.-H. Yoon, and B.-J. Kim, Chem. Mater. **32**, 4013 (2020).